GEM TN-92-128

FAST Simulation Meeting

June 30, 1992

Abstract:

Agenda, attendees, transparencies and draft reports from the final FAST Simulation Meeting, held at the SSCL, before the July 1992 PAC Meeting.

Agenda

Physics results from FAST1

FAST1 experience: lessons learned.

Future developments: FAST 2 ?

GEANT-based ?

PLAN OF PRESENTATION TO PAC

FAST Simulation Meeting 6/30/92

Name	Institution
Lee Roberts	SSCL
Jin Chu Wu	SSCL
Nasser Danesh	SSCL
Tomasz Skwarnicki	SSCL
Yu. Fisyak	—"—
Andrey Ostapchuk	—"—
Sasha Vanyashin	SSCL
Sumit Sen	YALE
I. Sheer	SSCL
Andrey Golutvin	SSCL
Frank Paige	SSC
KM McFarlane	SSCL
Larry Cormell	SSCL
Chiaki Yanagisawa	Stony Brook
Ren-yuan Zhu	Caltech.

gem

γeμ

Presentation by:

Chiaki Yanagisawa

Fast1 Simulation at Stony Brook.

Chiaki Yanagisawa
Stony Brook

§. $t\bar{t}$

- Signal

$$t\bar{t} \begin{cases} \to \bar{b}W^- \to e^-\bar{\nu} \\ \to bW^+ \begin{cases} \to e^+\nu \\ \to \mu^-\bar{\nu}c \end{cases} \end{cases}$$

isolated e
+
isolated μ
+
non-isolated μ

- Cuts

1) isolated electron

$$E_T(R<.2) > 20\,\mathrm{GeV}, \quad E_T(R<.3) - E_T^{em}(R<.2) < 5\,\mathrm{GeV}$$

$$E_e \equiv E(R<.2)$$

2) isolated muon

$$p_T > 20\,\mathrm{GeV}/c, \quad E_T(R<.2) - E_T(R<.1) < 5\,\mathrm{GeV}$$

3) non-isolated muon

$$p_T > 5\,\mathrm{GeV}/c, \quad E_T(R<.2) - E_T(R<.1) > 5\,\mathrm{GeV}$$

- Events generated
  - $50 < p_T^{top} < 1000$ GeV/c
  - 50k events for $m_t = 200, 250, 300$ GeV/c²
    10k 230, 270
  - Cross section × Br's
    18.9, 7.77, 3.65 pb for $m_t = 200, 250, 300$ GeV/c²
  - detection efficiency (identification eff. not included)
    20%, 26%, 32% for $m_t = 200, 250, 300$
  - # of events observed for $\mathcal{L} = 1 fb^{-1}$
    9500, 5104, 2932 events for $m_t = 200, 250, 300$.

- top quark mass measurement:
  measure $m_{e^\pm\mu^\mp}$ or $m_{\mu^\pm\mu^\mp}$

  $\langle m_{e^\pm\mu^\mp} \rangle = 47.1, 58.4, 66.4$ GeV/c²
  $m_t = 200, 250, 300$ GeV/c²

  $\Delta m_t = 1.9$ GeV/c² for $m_t = 250$ GeV/c².
  ↑ statistical only.

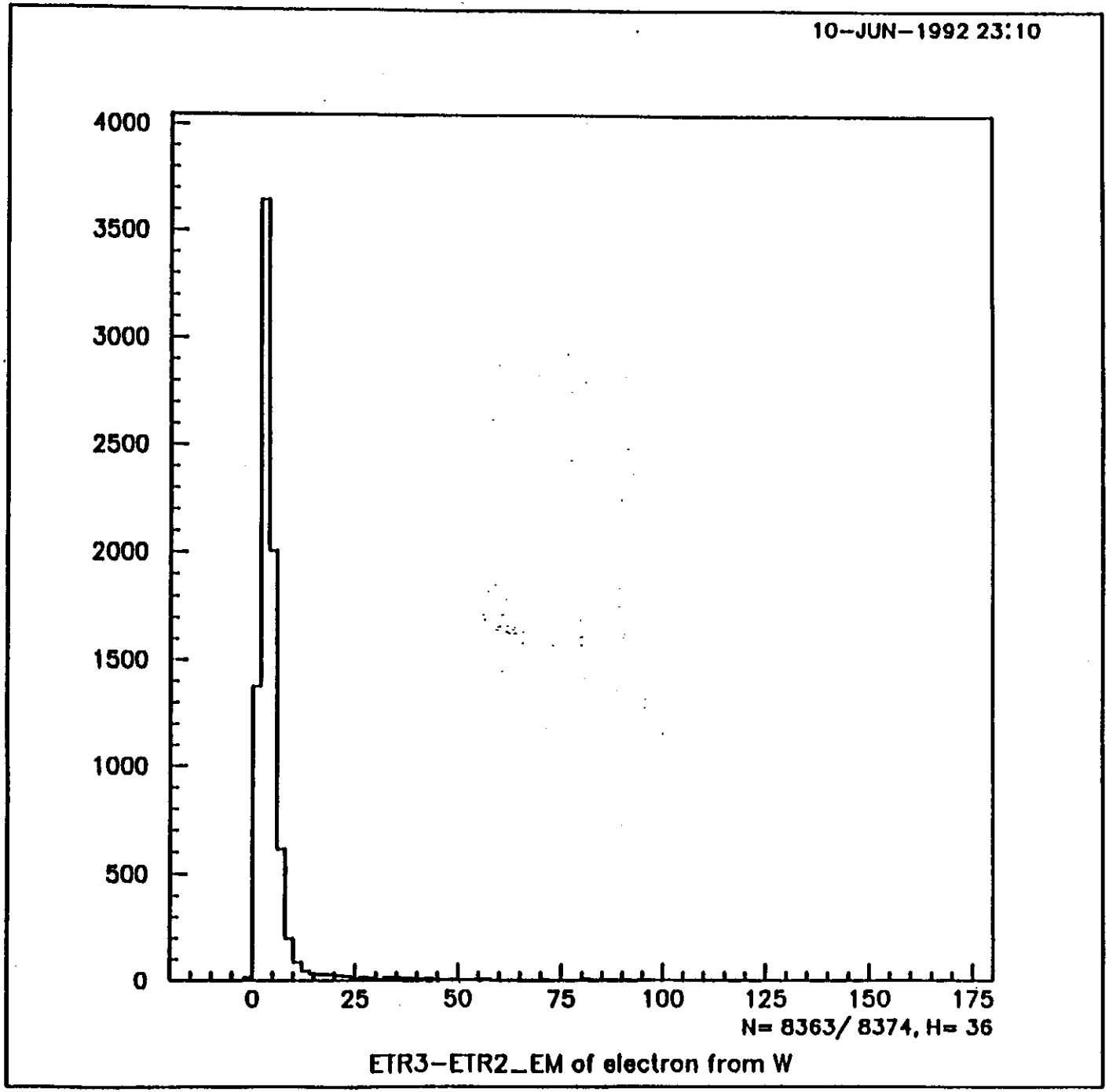
10-JUN-1992 23:10
4000
3500
3000
2500
2000
1500
1000
500
0
0
25
50
75
100
125
150
175
N= 8363/ 8374, H= 36
ETR3-ETR2_EM of electron from W

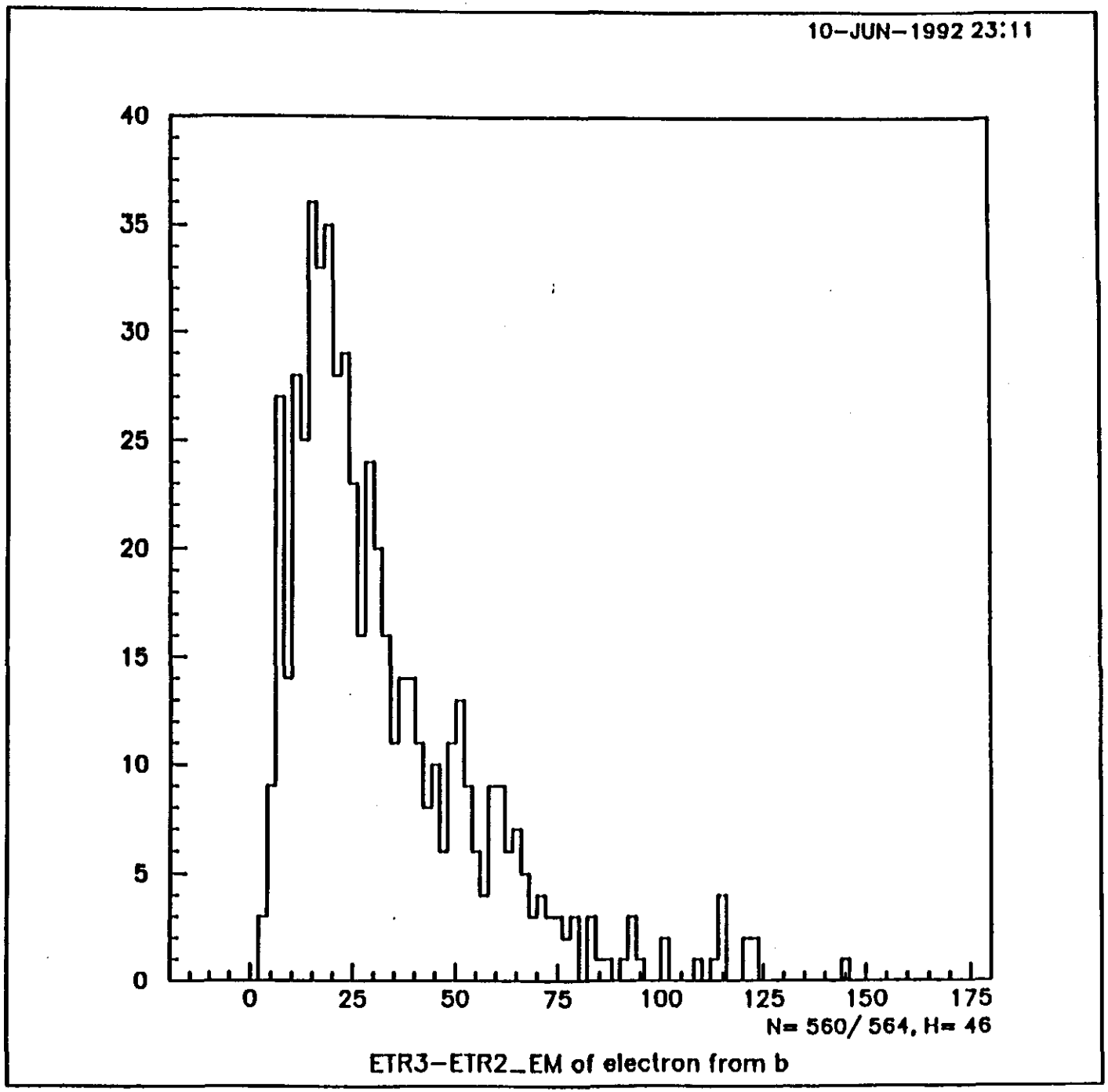
10-JUN-1992 23:11
40
35
30
25
20
15
10
5
0
0
25
50
75
100
125
150
175
N= 560/ 564, H= 46
ETR3-ETR2_EM of electron from b

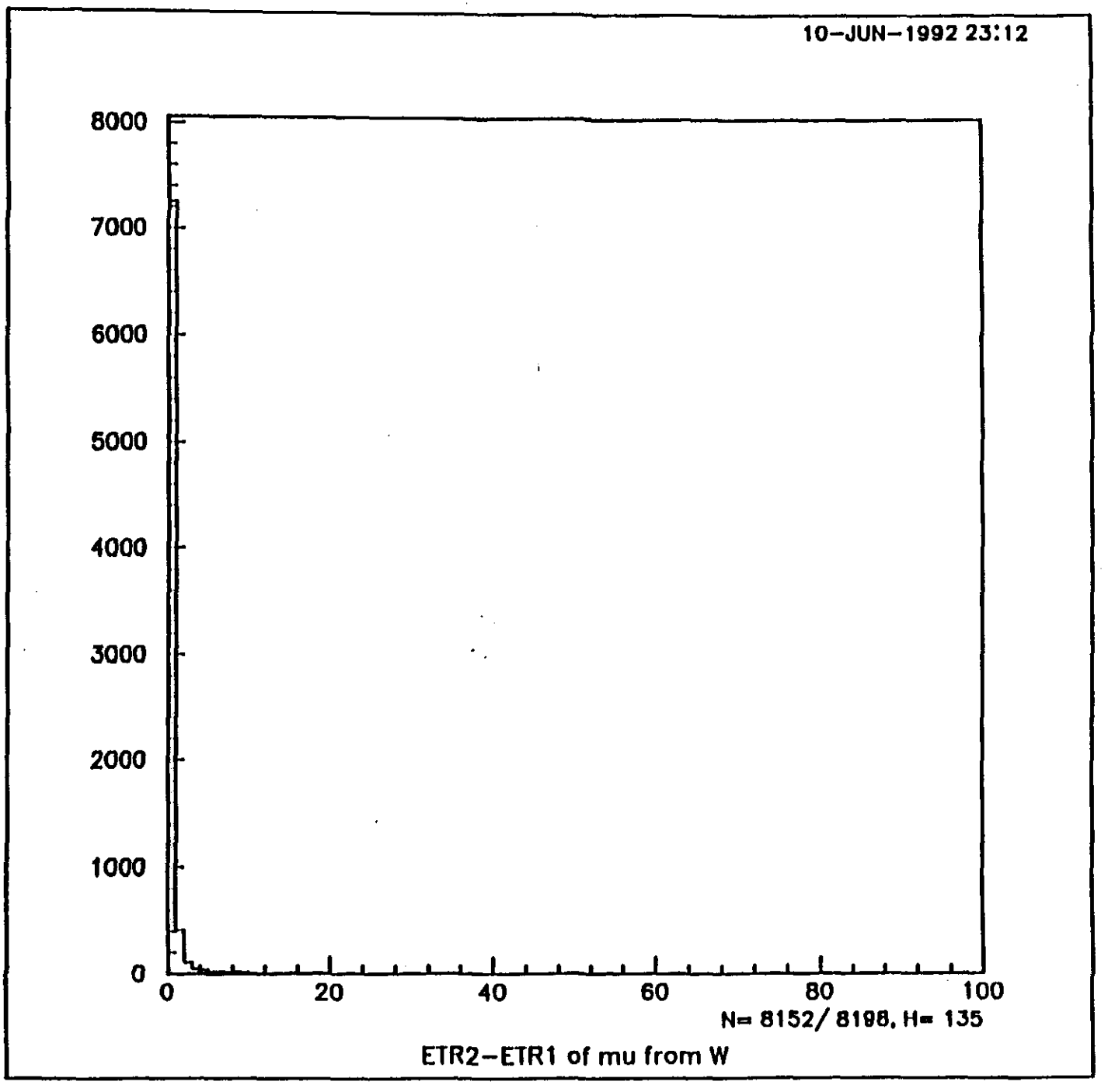
10-JUN-1992 23:12
8000
7000
6000
5000
4000
3000
2000
1000
0
0
20
40
60
80
100
N= 8152/ 8198, H= 135
ETR2-ETR1 of mu from W

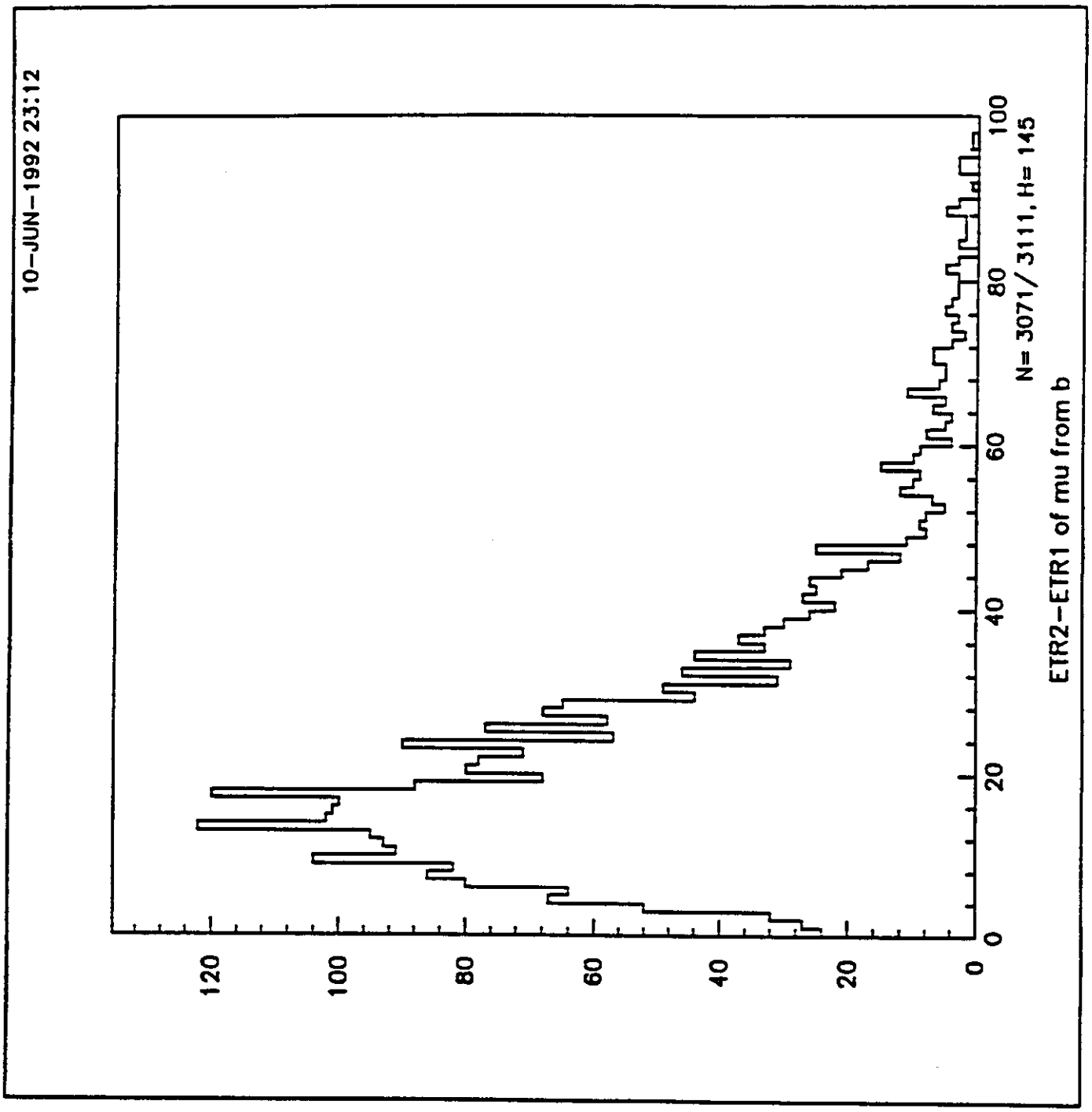
10-JUN-1992 23:12
120
100
80
60
40
20
0
0
20
40
60
80
100
ETR2-ETR1 of mu from b
N= 3071/ 3111, H= 145

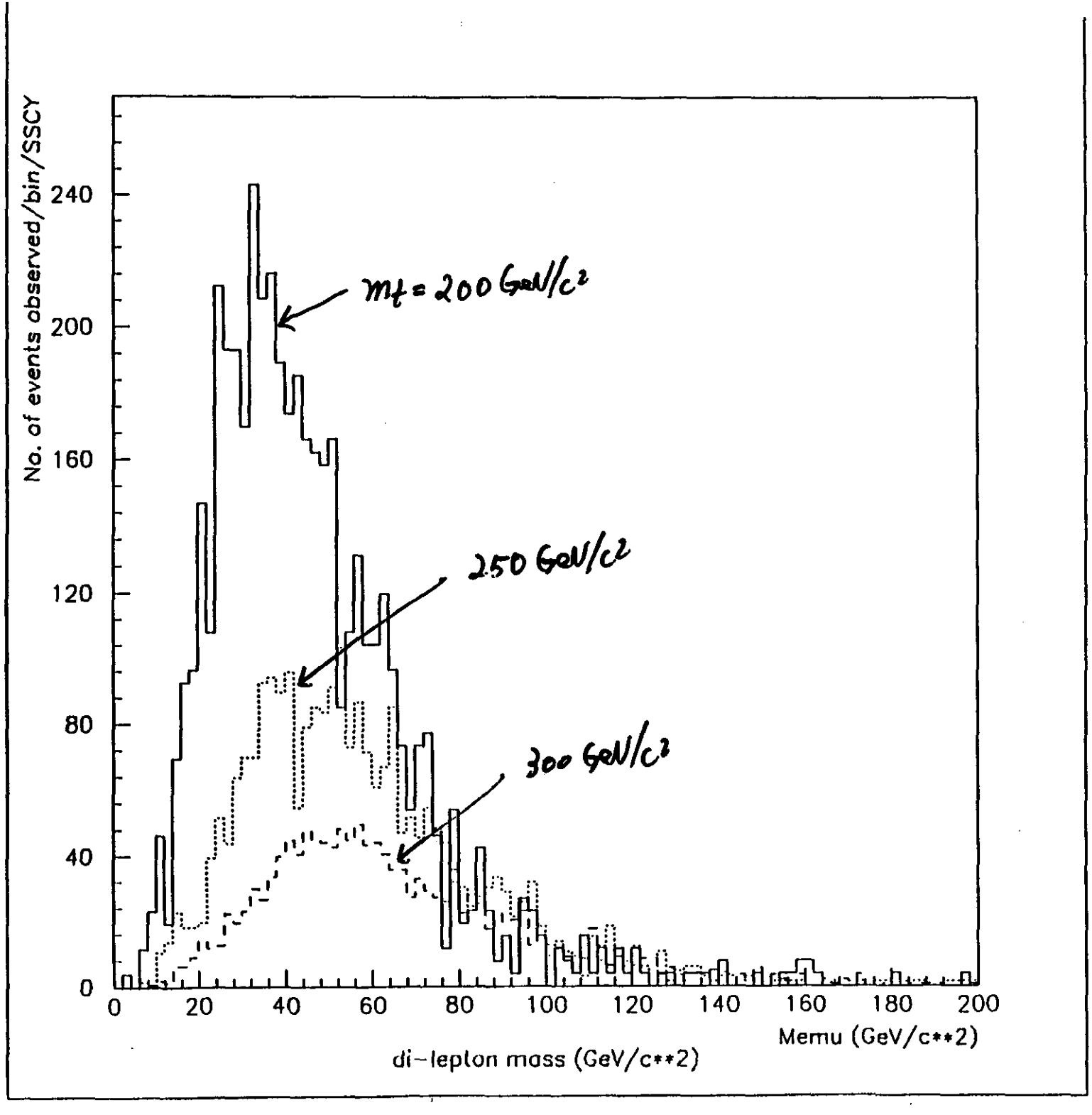
No. of events observed/bin/SSCY
240
200
160
120
80
40
0
0
20
40
60
80
100
120
140
160
180
200
Memu (GeV/c**2)
di-lepton mass (GeV/c**2)
mt = 200 GeV/c²
250 GeV/c²
300 GeV/c²

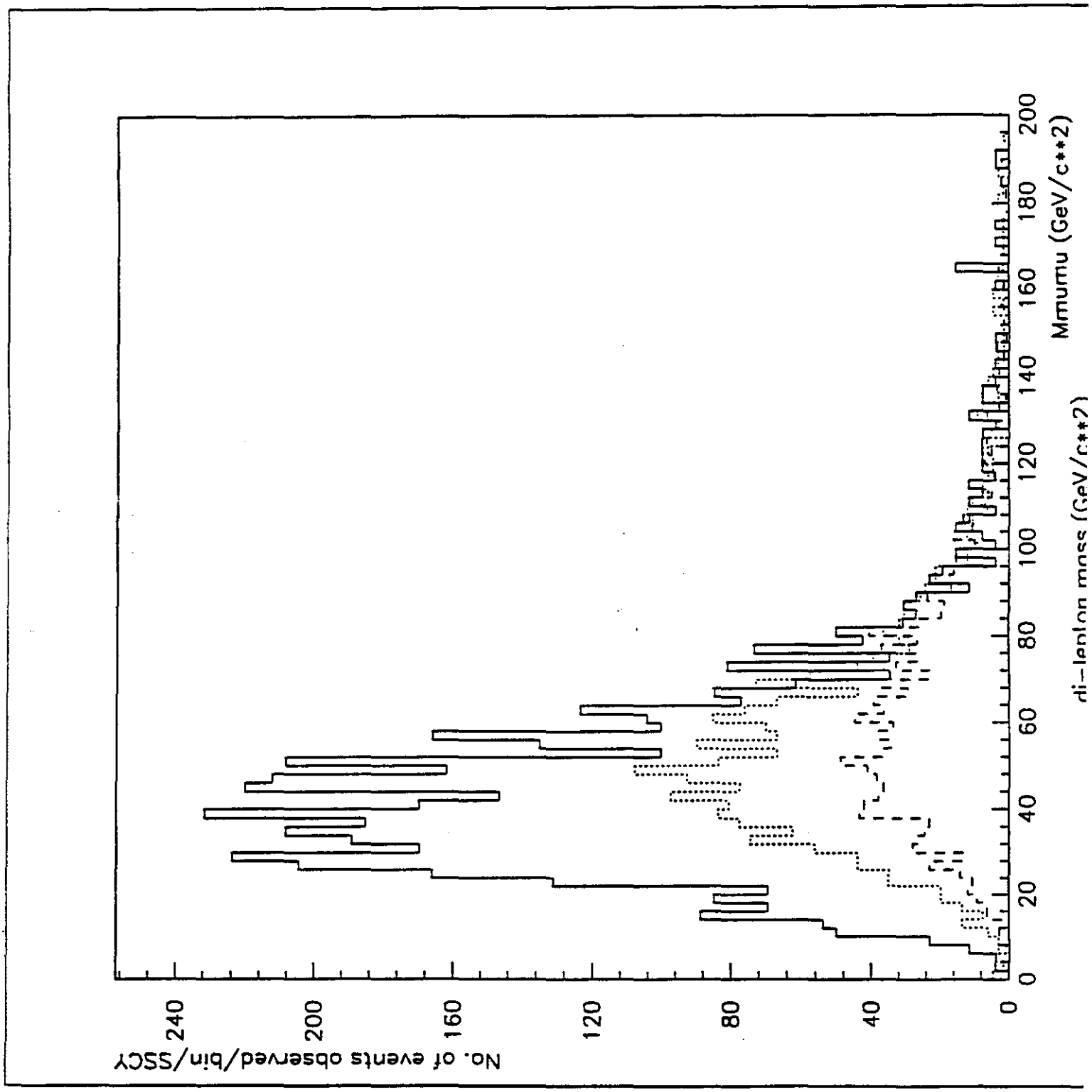
No. of events observed/bin/SSCY
0
40
80
120
160
200
240
0
20
40
60
80
100
120
140
160
180
200
Mmumu (GeV/c**2)
di-lepton mass (GeV/c**2)

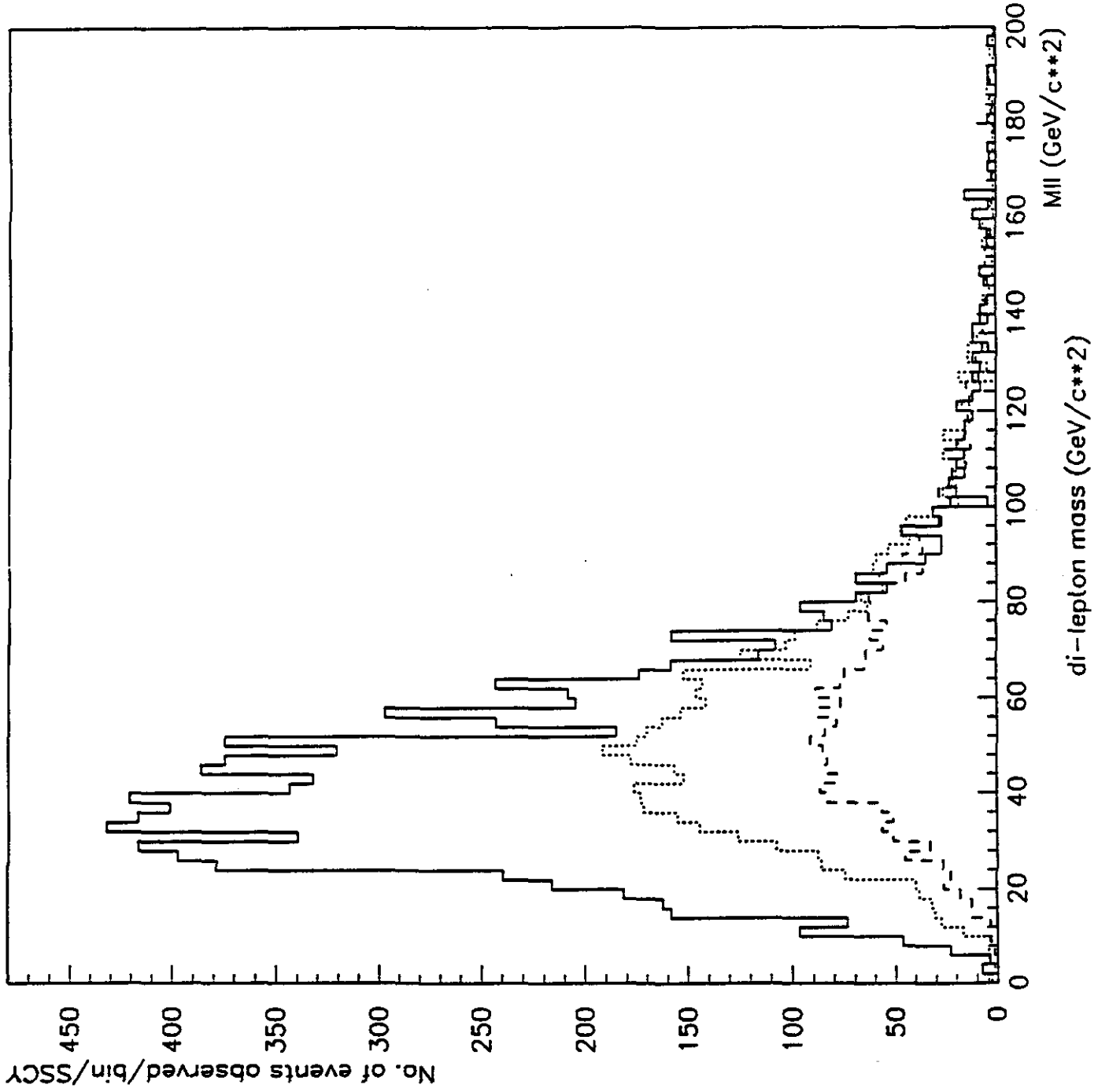
No. of events observed/bin/SSCY
450
400
350
300
250
200
150
100
50
0
0
20
40
60
80
100
120
140
160
180
200
di-lepton mass (GeV/c**2)
Mll (GeV/c**2)

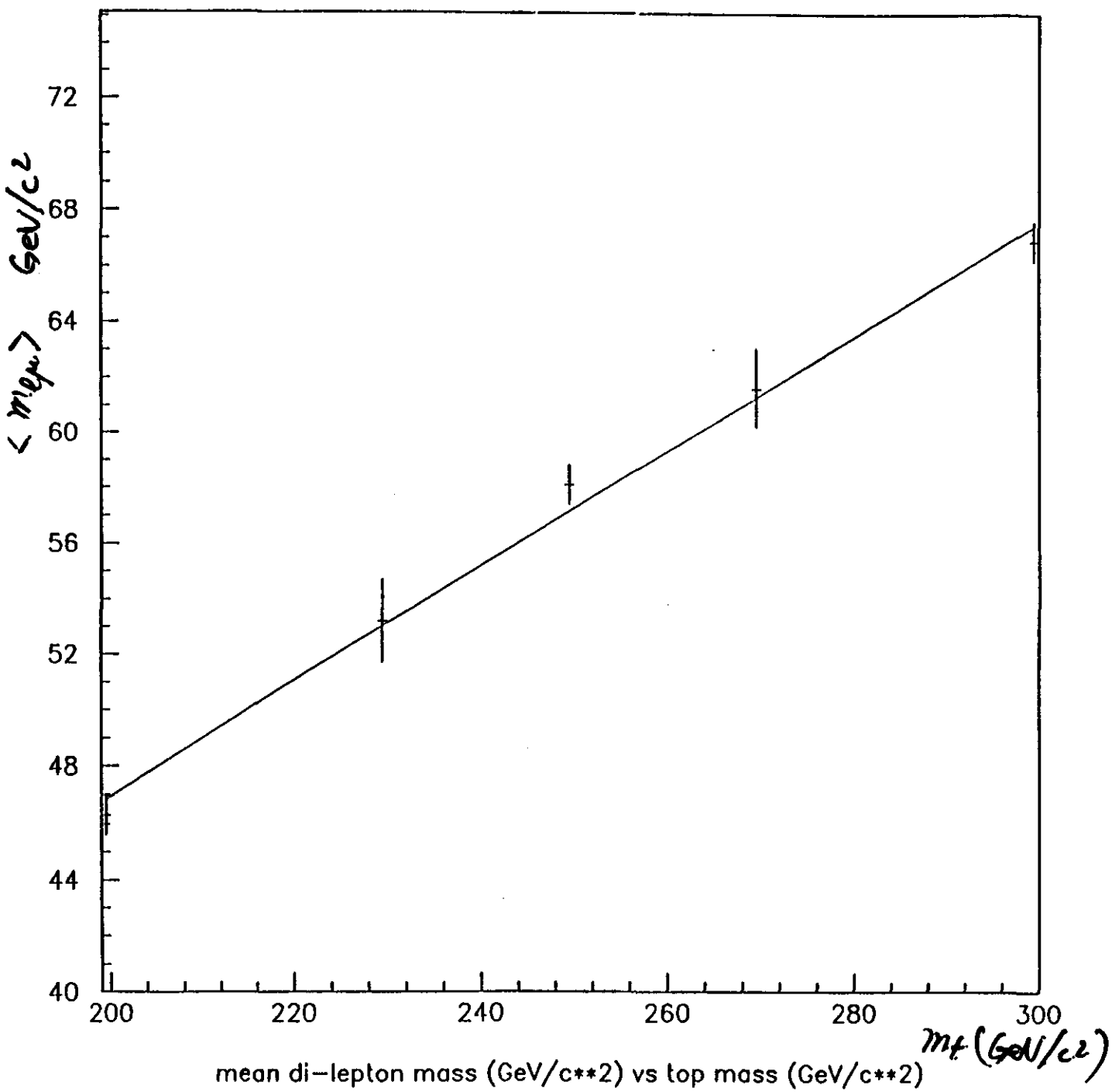
72
68
64
60
56
52
48
44
40
200
220
240
260
280
300
$\langle m_{\ell\mu} \rangle$ GeV/c²
m_t (GeV/c²)
mean di-lepton mass (GeV/c**2) vs top mass (GeV/c**2)

gem

γeμ

Presentation by:

Frank Paige

PAIGE

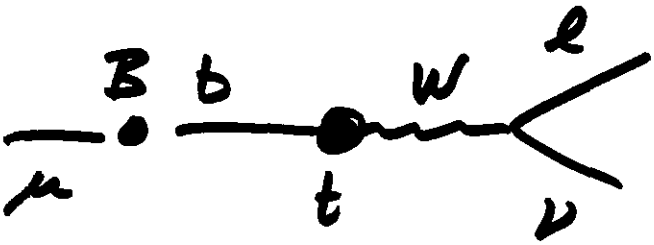

$$P_W = \frac{m_t^2 - m_W^2}{2m_t} \approx \frac{m_t}{2}$$

$W \to \ell\nu$: L : $\sin^2\theta^*$

T : $(1+\cos^2\theta^*)^2$

$$\frac{L}{T} = \frac{m_t^2}{2m_W^2}$$

$b \to B$: $f(x, Q^2 \simeq m_b^2)$

$B \to \mu$ only of m_t

§. $\tilde{g}\tilde{g} \to \ell^\pm \ell^\pm$

- Signal
  isolated
  like-sign dilepton $\mu^\pm\mu^\pm$, $e^\pm\mu^\pm$, $e^\pm e^\pm$

- Cuts.
  p_t, E_t and isolation cuts same as for $t\bar{t}$

- 50 k events generated ($m_{\tilde{g}} = 300\,\mathrm{GeV}/c^2$ $m_{\tilde{q}} = 600\,\mathrm{GeV}$
  $50 \le p_T \le 1000\,\mathrm{GeV}/c$
  - cross section 6.68 nb
  - 39 $\mu^\pm\mu^\pm$, 82 $e^\pm\mu^\pm$, 29 $e^\pm e^\pm$ observed.
  $\to$ 5.2k, 11.0 k, 3.9 k events/SSCY

- Background from $t\bar{t}$ with $m_t = 140\,\mathrm{GeV}/c^2$
  (50 k)
  - cross section 13.6 nb
  - 8 $\mu^\pm\mu^\pm$, 17 $e^\pm\mu^\pm$, 3 $e^\pm e^\pm$
  $\to$ 2.2k, 4.6 k, 0.8 k events/SSCY

gem

γeμ

Presentation by:

Lane

$M_{Z'} = 4\ \text{TeV}$ $\sim 10^{34} \times 10^{7}$.

2 modes $\longrightarrow$ $\Gamma_{Z'} \simeq$ 80 GeV, 120 GeV

$Z' \to e^+e^-$

800 GeV $H^0 \to Z^0 Z^0 \to e^+e^- \mu^+\mu^-$

GEM-TN-92-126

Draft

Intermediate Mass Higgs Searches with GEM Detector

$$H \rightarrow \gamma\gamma$$
$$H(t\bar{t}/W) \rightarrow (\mu/e)\gamma\gamma X$$
$$H \rightarrow e^+e^-e^+e^-$$

Ren-yuan Zhu and Hiro Yamamoto

Lauritsen Laboratory
California Institute of Technology
Pasadena, CA 91125

June 30, 1992

Part of a Physics Report to PAC

Abstract

This report summarises a study on signal and background for intermediate mass Higgs searches at SSC by using precision electromagnetic calorimeters proposed by GEM collaboration. Searches by using $H \rightarrow \gamma\gamma$, lepton associate production channel $H(t\bar{t}/W) \rightarrow (\mu/e)\gamma\gamma X$ and $H \rightarrow e^+e^-e^+e^-$ are discussed. Various physics as well as detector design issues were investigated The backgrounds from real photons and electrons and misidentified photons and electrons originated from jets are elaborated.

1 Introduction

As a precision lepton photon detector, the discovery potential of the GEM (Gamma-Electron-Muon) detector is shown in its ability of detecting Higgs particles in intermediate mass range between 80 and 180 GeV through its $\gamma\gamma$ and 4ℓ (ZZ^*) modes [1], where ℓ refers to electrom or muon (e/μ). While the 4ℓ decay mode will allow GEM to detect a Higgs with a mass heavier than 140 GeV, the $\gamma\gamma$ decay mode will cover a gap between the upper limit for Higgs detection at LEP Phase II (80 GeV) [2] and 140 GeV.

$H\rightarrow \gamma\gamma$ detection places strigent requirements to the overall detector design, especially to the design of the electromagnetic calorimeter (EMC). Because of the small production cross-section (60 to 200 fb) and the narrow decay width (5 to 10 MeV) of the Higgs boson in this mass range, and because of the huge irreducible direct $\gamma\gamma$ background (276 pb) and the QCD jet background, precision EMCs, capable of measuring $\gamma\gamma$ invariant mass to a high precision, are pursued by GEM. Two subsystems were proposed: a barium fluoride (BaF_2) crystal calorimeter and a liquid argon (LAr) accordion calorimeter with liquid krypton (LKr) option.

The main course of this note reports a study on signal and background of Higgs searches by using $H\rightarrow \gamma\gamma$ channel. Large fraction of this work, including $Ht\bar{t} \rightarrow \ell\gamma\gamma$, was carried out for GEM LoI study, and has been reported in a GEM note [3]. The analysis, since then, has been suplemented by additional studies to address a broder range of physics issues.

The background from real photons and electrons, as well as misidentified photons and electronsfrom jets are investigated. For jet background rejection, the consequence of thermal as well as pile-up noise in an isolation cone is discussed. Intermediate mass Higgs detection by using lepton associate production channel $H(t\bar{t}/W)\rightarrow (\mu/e)\gamma\gamma$ and $H\rightarrow e^+e^-e^+e^-$ are also discussed.

The Monte Carlo program used in this study is PYTHIA 5.6 [4], and the top quark mass is assumed to be 140 GeV. An SSC year (SSCY) is defined as 10^{40} cm^{-2} integrated luminosity.

2 γ/e Response of GEM EM Calorimeters

The responses of GEM detector to isolated photons or electrons were simulated according parametrized energy, position and vertex z resolutions. The parametrization was obtained by using rigorous GEANT simulations for each proposed subsystems [5,6]. Key parameters of detector performance were varied to investigate their influences on physics performance.

In this section we discuss the parametrization of energy resolution and detector coverage. A global parametrization of GEM detector response used in event acceptance and jet background study is also described in this section. The detailed procedure of GEANT simulation and justification of all parameters used in analysis can be obtained in corresponding GEM notes: reference [5] for BaF_2 simulation and reference [6] for LAr simulation. In a short summary, the parametrization of detector performance is as follows:

- **Energy Resolution:**
  - $(2.0/\sqrt{E} \oplus 0.5)\%$ for homogeneous BaF_2 calorimeter; and
  - $(7.5/\sqrt{E} \oplus 0.5)\%$ for LAr accordion and $(5.5/\sqrt{E} \oplus 0.5)\%$ for LKr accordion.
- **Position Resolution:** $\delta x = \delta y = 1$ mm at front surface of EMC are used for both calorimeters;
- **Vertex z Resolution:** $\delta z = 1$ mm are used for both calorimeters. Photon momentum vector is assumed to be reconstructed by using primary vertex position and its impact point at front surface of the EMC, while the primary event vertex is assumed to be determined by using central tracker at standard SSC luminosity $\mathcal{L} = 10^{33}$ cm^{-1} s^{-1} (see section 3.6 for the details).

2.1 Parametrization of γ/e Energy Resolution

The energy resolution of an electromagnetic calorimeter can be parametrized as:

$$(\frac{\Delta E}{E})^2 = (\frac{a_0}{E})^2 + (\frac{a_1}{\sqrt{E}})^2 + b^2 \tag{1}$$

The contributions of each term to the resolution are:

- $\mathbf{a_0}$ is the contribution from electrical noise, summed over a few Moliere radii around the maximum of the lateral shower distribution;
- $\mathbf{a_1}$ is the contribution from the photoelectron statistics;
- the systematic term b has three contributions:

$$\mathbf{b^2 = b_n{}^2 + b_G{}^2 + b_C{}^2} \tag{2}$$

  - $\mathbf{b_G}$ represents the geometry effect, including shower leakage at the front, side and back of the detector and inactive material between cells;
  - $\mathbf{b_n}$ represents physics noise, including fluctuations of the shower and uniformity of cell response etc.;
  - $\mathbf{b_C}$ represents intercalibration error.

At low energy, the dominant contribution to the energy resolution is the noise term ($\mathbf{a_0}$), which decreases quickly with increasing energy. The sampling term ($\mathbf{a_1}$) dominates in the range of medium to high energies until a high energy limit is reached, where the systematic term (b) dominant. While most numbers can be calculated analytically, the effect of $\mathbf{b_G}$ and $\mathbf{b_n}$ must be studied with realistic GEANT simulation. Assuming $\mathbf{b_n}$ is under control, a simple GEANT simulation can provide a bottom line resolution the EMA can achieve.

In this report, we parametrize the energy resolution of an EMC as a function of parameters a and b:

$$\frac{\Delta E}{E} = (\frac{\mathbf{a}}{\sqrt{\mathbf{E}}} \oplus \mathbf{b})\% \tag{3}$$

where $\oplus$ denotes an addition in quadrature.

2.1.1 BaF_2 Simulation

A detailed GEANT simulation was carried out to estimate the effect of shower leakage and non-active material for the BaF_2 design [5]. The BaF_2 matrix used in this simulation, which consists of 121 (11 × 11) BaF_2 crystals with the proposed size: 3 × 3 cm^2 at the front, 5 × 5 cm^2 at the back and 50 cm long. Effects included in the simulation are:

- 250 μm carbon fiber wall between crystals;

- shower leakage because of summing a limited number (3×3 or 5×5) of crystals; and
- 0.30 radiation lengths of aluminum, representing the beam pipe, tracker, and carbon fiber mechanical support, at the front of the BaF_2 array.

Particles were shoot uniformly at the front surface of the center crystals of the array. The energies deposited in each crystal, in the carbon fiber walls between crystals, in the aluminum and leaking out sideways were recorded. The result of this simulation for electrons with different energies (5, 10, 100 ad 500 GeV), in terms of σ of the peak, full width at half maximum (FWHM) divided by 2.35, is listed in Table 1.

Table 1: Energy Resolution (%) of BaF_2 Calorimeter

E (GeV)	5	10	20	50	100	200	500
Electrical Noise	0.4	0.2	0.1	0.04	0.02	0.01	0.004
Photoelectrons	0.2	0.14	0.1	0.063	0.045	0.03	0.02
GEANT	0.60	0.43	0.32	0.30	0.30	0.30	0.36
Intercalibration	0.40	0.40	0.40	0.40	0.40	0.40	0.40
Total	0.85	0.63	0.53	0.51	0.50	0.50	0.54

A further study was carried to look the systematic effect of carbon fiber wall. By varying the thickness of carbon fiber walls from 0 to 250 μm, the resolution obtained showed no observable difference [5]. This indicates that the systematic effect of support structure is negligible.

Table 1 summarizes the BaF_2 resolution, including the contributions from electrical noise, photoelectron statistics, intrinsic resolution from GEANT simulation and the intercalibration. Based upon the discussion in reference [5], a precision of intercalibration of 0.4% is assumed. Note, in this simulation the light response uniformity was assumed to be under control. The real effect of light response uniformity is discussed in reference [5]. The result of the energy resolution is shown in Fig. 1b. It can be parametrized as $2\%/\sqrt{E} \oplus 0.5\%$, which is also shown in Fig. 1b as a solid line.

As a comparison, Fig. 1a shows the energy resolution measured with 4000 BGO crystals (half barrel) in a CERN test beam [7]. In the energy range beyond 20 GeV, the dominant contribution to the energy resolution is the systematic intercalibration

uncertainties. The resolution of the L3 BGO calorimeter may also be parametrized as $2\%/\sqrt{E} \oplus 0.5\%$, which is also shown in the Fig. 1a as a solid line.

2.1.2 LAr Simulation

As detailed in reference [6], an accordion geometry was used in GEANT simulation to evaluate the intrinsic resolution of LAr calorimeter. The result shows that at 90° incident the energy resolution of LAr accordion calorimeter with 1 mm Pb plate can be parametrized as $\mathbf{a} = 7$ in Equation 3.

A study on incident angle dependence shows that the energy resolution of LAr calorimeter is about the same at $|\eta| = 1$ but rises to $\mathbf{a} = 8.5$ at $|\eta| = 1.3$ for a constant plate thickness. However, we plan to change the thickness of the absorber plate at a convenient angle to keep the resolution at $|\eta| = 1.3$ to be about the same value as at $\eta = 0$.

Taking into account of various systematics in Equation 1, we thus use $\mathbf{a} = 7.5$ and $\mathbf{b} = 0.5$ for parametrization of LAr energy resolution. This resolution can be further improved by replacing liquid argon with liquid krypton. In this case, the study shows that $\mathbf{a} = 5.5$ and $\mathbf{b} = 0.5$ are the design goal.

2.2 γ/e Acceptance

The detailed design of GEM calorimeters is evolving in time. A realistic estimation of γ/e acceptance may only be provided after the completion of detailed design of the calorimeter. Here we discuss general principle of our treatment of acceptance problem. Both geometry accptance and e/γ identification efficiency are discussed in this section.

Although both calorimeter options are designed to cover up to $|\eta| < 3.0$, the effective geometry acceptance is $|\eta| < 2.5$ because of the rapidity coverage of GEM central tracker. In both BaF_2 and LAr calorimeters, there are dead spaces and regions where the energy resolution is extremely bad. In the following rapidity regions, the energy resolution is expected to be very bad, or EM energy may not be measured at all:

- BaF_2 $|\eta| = 0 - 0.0125$ and $|\eta| = 1.348 - 1.388$;
- LAr $|\eta| = 1.22 - 1.39$.

When an electron or γ hits the calorimeter close to these dead regions, some of the showers leak into the dead region, and large corrections might be necessary. The exact effect on energy resolution in these region can only be investigated by using detailed GEANT simulation. A most pessimistic estimation of this effect, however, may be obtained by excluding the boundary and its vicinity of $\Delta\eta = \pm\ 0.04$ if the boundary has dead material in its neighbour. We thus have the following dead regions:

- BaF_2 $\quad |\eta| = 0 - 0.0525$ and $|\eta| = 1.308 - 1.428$;
- LAr $\quad |\eta| = 1.18 - 1.39$.

The effect of these dead regions was studied to investigate the overall physics acceptance for $H \to \gamma\gamma$, $Ht\bar{t} \to \gamma\gamma\ell$ and $H \to e^+e^-e^+e^-$. Assuming the muon acceptance is 90%, Table 2 shows the result of geometry acceptance (GA) by using our standard event selection cuts (see below for the details) for these physics processes. For each calorimeter option both optimistic (O) and pessimistic (P) dead region assumptions were investigated, and the event is accepted if none of the γ/e hits the dead region.

Table 2: Geometry Acceptance (GA) of GEM EM Calorimeters

Process	BaF_2 (O)	BaF_2 (P)	LAr (O)	LAr (P)	Abs. Efficiency
$H \to \gamma\gamma$	0.95	0.86	0.87	0.83	0.49
$Ht\bar{t} \to \gamma\gamma\mu X$	0.86	0.77	0.77	0.74	0.16
$Ht\bar{t} \to \gamma\gamma eX$	0.93	0.81	0.79	0.74	0.16
$H \to ZZ^* \to 4e$	0.91	0.75	0.73	0.67	0.45
$H \to ZZ \to 4e$	0.90	0.74	0.74	0.68	0.50

The geometry acceptance listed in Table 2 does not depend on the Higgs mass, and is entirely determined by the number of electrons or gammas being detected. The last column of Table 2 is the average absolute event selection efficiency, assuming no dead region in $|\eta| < 2.5$. This efficiency, however, is Higgs mass dependent. The numbers given here are for a quick reference purpose.

It is clear from above table, that the effect on acceptance caused by dead region in calorimeter can be understood as

$$\left(\frac{5. - \Delta\eta(dead)}{5.}\right)^{\#\ e's\ and\ \gamma's\ to\ detect} \tag{4}$$

The average geometry acceptance of most optimistic and pessimistic cases is listed in Table 3. Assuming 90% identification efficiency for each μ, e and γ, Table 3 also lists the final relative acceptance (RA) for each physics process. Since this relative acceptance is applied to both signal and background, its real consequence in discovery potential is a loss of significance of $\sqrt{RA}$ (see Equation 5 for the details), or an increase of discovery time of 1/RA.

Table 3: Average GA and Final Relative Acceptance (RA)

	Average GA		RA	
Process	BaF_2	LAr	BaF_2	LAr
$H \rightarrow \gamma\gamma$	0.90	0.85	0.73	0.69
$Ht\bar{t} \rightarrow \gamma\gamma\mu X$	0.82	0.76	0.60	0.55
$Ht\bar{t} \rightarrow \gamma\gamma eX$	0.87	0.77	0.63	0.56
$H \rightarrow ZZ^* \rightarrow 4e$	0.83	0.70	0.54	0.46
$H \rightarrow ZZ \rightarrow 4e$	0.82	0.71	0.54	0.47

To facilitate compariosn, this relative acceptance has not been applied to the tables and figures in this report. Its consequence on signal significance, however, is discussed for each physics process.

2.3 Parametrized Response of Calorimeters

For event acceptance and jet background rejection calculation, a parametrized response of ideal calorimeter systems was used. The ideal calorimeters were defined in $|\eta| < 2.5$, and were segmented to $\Delta\eta \times \Delta\phi = 0.04 \times 0.04$ in both EMC and hadron calorimeter (HCAL) sections. No longitudinal segmentation in EMC or HCAL was assumed.

The longitudinal energy division between EMC and HCAL was assigned based upon a GEANT study for BaF_2 calorimeter [8]. All γ/electrons have 100% of their energies deposited in EMC. All muons are minimum ionizing, i.e. deposit minimum ionizing energy (MIE) in EMC. For charged hadrons, if its energy is less than 2 MIE then all its energy were deposited in EMC, otherwise it has 25% probability of depositing MIE in EMC, and 75% probability of depositing a fraction of its energy in EMC with the rest in HCAL. This fraction was determined according to a uniform

distribution between MIE and about 80% of the energy of the hadron.

The energies deposited in EMC and HCAL were further divided to 50 pieces and deposited to cells according to lateral shower profile. This process provides a first order approximation of lateral energy distribution in EMC/HCAL cells, and is used in calculations of our detector acceptance and jet background rejection. It was also used in a trigger rate study [8].

3 Signal and Irreducible Background

3.1 Signal Cross Section

Figure 2 shows the production cross-sections of standard model Higgs in three interesting decay modes: (a) $\gamma\gamma$, (b) $(t\bar{t}/W)H \rightarrow \gamma\gamma\ell$ X, and (c) $ZZ^*/ZZ \rightarrow e^+e^-e^+e^-$, before event selection cuts. These cross sections were calculated by using PYTHIA 5.6 program.

For the Higgs mass range between 80 to 150 GeV, the $\gamma\gamma$ decay mode provides 1200 to 2100 events per SSC year, while $t\bar{t}H \rightarrow \gamma\gamma\ell X$ together with $WH \rightarrow \gamma\gamma\ell X$ provide 80 to 240 events without lepton tagging, or 20 to 80 events with electron or muon tagging. The 4 electron decay channel ($ZZ^*/ZZ \rightarrow e^+e^-e^+e^-$) provides 20 to 30 events per SSC year. Combining electron and muon, 80 to 120 would be produced before cuts. Table 4 lists production cross-section and number of events accepted after passing event selection cuts described in this report. Note, the event numbers listed in this table are for a perfect calorimeter, covering $|\eta| < 2.5$. The acceptance loss discussed in section 2.2 is not included in the table.

Taking into account a recent calculation of high order QCD corrections to the Higgs production [9], the production cross sections of $H \rightarrow \gamma\gamma$ and $H \rightarrow ZZ^*/ZZ \rightarrow e^+e^-e^+e^-$ should be increased by a K factor of around 1.5 for Higgs mass below $t\bar{t}$ threshould. However, since we do not have a consistent picture of high order QCD corrections to the background processes, we choose not to change the signal cross section in this report. The consequence of this increase of signal cross section to the significance of the physics signal will also be discussed individually for each relevant physics process.

3.2 Irreducible $\gamma\gamma$ Background

The main background in $H \rightarrow \gamma\gamma$ searches is direct photon production [10]. The cross-section of this background was calculated to be 276 pb for $\hat{p}_T > 20$ GeV:

- $q\bar{q} \rightarrow \gamma\gamma$: 78 pb; and
- $gg \rightarrow \gamma\gamma$ via a box diagram: 198 pb.

Table 4: Production Cross-Section and Events/SSCY

M_H(GeV)	$\sigma_{H(\gamma\gamma)}(fb)$	$N_{\gamma\gamma}$	$\sigma_{(t\bar{t}/W)H(\gamma\gamma)}$ (fb)	$N_{l\gamma\gamma}$	$\sigma_{H(4e)}(fb)$	N_{4e}
80	124	510	24	18		
90	144	610	23	20		
100	169	730	23	21		
120	211	990	20	18		
140	180	880	12.5	14	5.6	24
150	128	630	7.6	8	7.4	33
160	52.6	270	2.6	3	3.2	13
170					2.2	9
180					5.6	28
200					21.2	99
400					14.0	85
600					3.9	26
800					1.5	10

The event topology of H$\rightarrow \gamma\gamma$ and this background are similar. Figure 3 shows transverse energy distributions in EMC for two typical events of (a) H$\rightarrow \gamma\gamma$ signal and (b) $\gamma\gamma$ background. This so-called *"irreducible background"* therefore has to be reduced by event selection cuts. Figure 4 shows the distributions of photon rapidity (η_γ), photon transverse energy (E_T^γ), rapidity of the 2 photon system ($\eta_{\gamma\gamma}$) and cosθ^*, where θ^* is the polar angle of photons in the $\gamma\gamma$ rest frame, for H$\rightarrow \gamma\gamma$, q$\bar{q} \rightarrow \gamma\gamma$ and gg $\rightarrow \gamma\gamma$.

Event selection cuts used to reduce this background are:

- $|\eta_\gamma| < 2.5$;
- $E_T > 20$ GeV;
- $|cos\theta_\gamma^*| < 0.9 \Rightarrow$ reduce gg $\rightarrow \gamma\gamma$;
- $|\eta_{\gamma\gamma}| < 3 \Rightarrow$ reduce qq $\rightarrow \gamma\gamma$.

After event selection cuts, the cross-section of irreducible background is reduced to 42 pb for $M_{\gamma\gamma} > 75$ GeV, while the acceptance of $H \rightarrow \gamma\gamma$ events is about 50%.

3.3 Significance of Higgs Peaks

Because of large numbers of irreducible background events, the significance (S) of Higgs peaks can be calculated by dividing the number of signal events counted within a mass interval of $M_H \pm \sigma_{M_{\gamma\gamma}}$ by the square root of the corresponding background events in the same mass interval, where $\sigma_{M_{\gamma\gamma}}$ is the $\gamma\gamma$ invariant mass resolution. We thus have

$$S = \frac{N_S}{\sqrt{N_B}} = \frac{\int \mathcal{L}dt\ A_S\ RA\ 0.7\sigma_{H\rightarrow\gamma\gamma}}{\sqrt{\int \mathcal{L}dt\ A_B\ RA\ 2\sigma_{M_{\gamma\gamma}}\ R_B}} \propto \sqrt{\frac{RA \int \mathcal{L}dt}{\sigma_{M_{\gamma\gamma}}}} \tag{5}$$

where A_S and A_B are the absolute accceptance of signal and background respectively, RA is the relative acceptance discussed in section 2.2, and R_B is the background rate at Higgs mass. It is clear from Equation 5 that a better mass resolution or a large relative acceptance is equivalent to a shorter discovery time.

3.3.1 $\gamma\gamma$ Mass Resolution

Analytically, the mass resolution reconstructed by using two photon energy vectors can be expressed as:

$$\frac{\sigma_{M_{\gamma\gamma}}}{M_{\gamma\gamma}} = \frac{1}{2}\sqrt{(\frac{\Delta E_1}{E_1})^2 + (\frac{\Delta E_2}{E_2})^2 + (\cot\frac{\theta}{2}\Delta\theta)^2} \tag{6}$$

where E_1 and E_2 are energies of two photons and θ is the opening angle between them.

In this analysis, mass resolution was calculated by using Higgs events passing event selection cuts. Events were generated by using PYTHIA 5.6 program. The primary event vertex position and photon impact point at front surface of the EMC were used to reconstruct the photon momentum vectors, taking into account the effects of energy resolution assumed, 1 mm position resolution at the front surface of EMC and 1 mm vertex z resolution. It was assumed that the primary event vertex can be determined by using central tracker at standard SSC luminosity 10^{33} cm^{-2} s^{-1} (see section 3.6 for the details).

3.3.2 Significance

Figure 5 shows $\gamma\gamma$ invariant mass spectra collected in one SSCY with Higgs signals (80, 100, 120, 140 and 160 GeV) superimposed over the irreducible background for three energy resolutions: (a) $(2/\sqrt{E} \oplus 0.5)\%$; (b) $(7.5/\sqrt{E} \oplus 0.5)\%$; and (c) $(15/\sqrt{E} \oplus 1)\%$. Corresponding background subtracted spectra are shown in (d), (e) and (f).

Table 5 summarizes production cross-section and number of signal events (N_S) in $M_H \pm \sigma_{M_{\gamma\gamma}}$ for different Higgs masses. Also listed in Table 5 are mass resolutions ($\sigma_{M_{\gamma\gamma}}$) and significances (S) for three nominal energy resolutions.

Table 5: Significance of H$\rightarrow \gamma\gamma$ Searches in one SSCY

$\Delta E/E$ (%)			$2/\sqrt{E} \oplus 0.5$		$7.5/\sqrt{E} \oplus 0.5$		$15/\sqrt{E} \oplus 1.0$	
M_H (GeV)	$\sigma_{\gamma\gamma}$ (fb)	N_S	$\sigma_{M_{\gamma\gamma}}$ (GeV)	S	$\sigma_{M_{\gamma\gamma}}$ (GeV)	S	$\sigma_{M_{\gamma\gamma}}$ (GeV)	S
80	124	360	0.34	4.6	0.66	3.2	1.3	2.3
90	144	430	0.37	6.1	0.70	4.5	1.4	3.2
100	169	510	0.40	8.6	0.73	6.3	1.45	4.5
120	211	690	0.45	14	0.77	11	1.5	7.7
140	180	620	0.53	16	0.89	12	1.7	8.9
150	128	450	0.58	13	0.95	10	1.9	7.3
160	52.6	190	0.65	5.9	1.1	4.7	2.0	3.4

Note, the event numbers listed in this table and in Figure 5 are for a perfect EMC without including the acceptance loss discussed in section 2.2. Taking into account the relative acceptance listed in Table 3, the numbers of both signal and background events should be reduced to 73% and 69% respectively for BaF_2 calorimeter and LAr calorimeters. The corresponding significance should be reduced to 85% and 83% respectively.

On the other hand, taking into account high order QCD corrections to the Higgs production [9], i.e. the K factor of 1.5, the corresponding numbers of signal events and significance should both be increased by a factor of 1.5. This might really be the case, since the dominant irreducible background process of gg$\rightarrow \gamma\gamma$ is an $O(\alpha_s^2)$ process.

Table 5 shows clearly the importance of excellent energy resolution in pursuing

this physics. In summary, there is a factor of $\sqrt{1.8}$ difference in significances of H$\rightarrow \gamma\gamma$ detection, or a factor of 1.8 difference in time needed to achieve certain significance, between two neighboring energy resolutions in above table.

According to Equation 5, an easy way to evaluate detector performance in terms of physics discovery potential is to look its $\gamma\gamma$ mass resolution. In the rest of this section, we discuss the consequences of probable deviations from designed resolutions.

3.4 Effect of Energy Resolution

To study systematically the effect of energy resolution, we parametrize the energy resolution of an EMC as a function of parameters **a** and **b**, as defined in Equations 3. The result of this analysis, listed in Table 6, shows the ratio of H$\rightarrow \gamma\gamma$ peak width as a function of energy resolution (**a** and **b**), normalized to the case of **a** = 2 and **b** = 0.5, for Higgs mass of 80 GeV and 150 GeV. Because of the high statistics of the background, this ratio corresponds to the time factor needed to discover a narrow $\gamma\gamma$ resonance, as indicated in Equation 5.

Table 6: Ratio of H$\rightarrow \gamma\gamma$ Peak Width as Function of **a** and **b**.

a	2.0	3.0	5.5	7.5	10	15
M_H = 80 GeV						
b=0.5	1.0	1.1	1.5	1.9	2.4	3.4
b=.75	1.4	1.5	1.7	2.1	2.6	3.6
b=1.0	1.8	1.8	2.1	2.4	2.8	3.8
b=1.5	2.6	2.6	2.8	3.1	3.4	4.2
b=2.0	3.4	3.5	3.6	3.8	4.1	4.8
M_H = 150 GeV						
b=0.5	1.0	1.1	1.3	1.6	2.0	2.8
b=.75	1.4	1.5	1.7	1.9	2.3	3.0
b=1.0	1.8	1.9	2.0	2.2	2.5	3.2
b=1.5	2.6	2.7	2.8	3.0	3.2	3.7
b=2.0	3.6	3.6	3.7	3.8	4.0	4.4

3.5 Effect of Position Resolution

It is also interesting to see the effect of shower position resolution. Table 7 shows the ratio of H→ $\gamma\gamma$ peak width as a function of the shower position resolution (δx) and energy resolution (a and b), for Higgs mass of 80 GeV. The numbers in the table are normalized to the case of a = 2, b = 0.5 and δx = δy = 1 mm. It is clear that the shower position resolution of the order of few mm will not compromise the discovery potential of a precison EM calorimeter.

Table 7: Ratio of H→ $\gamma\gamma$ Peak Width as Function of δx, a and b.

δx (mm)		0.5	1.0	1.5	2.0	2.5	3.0
a=2	b=0.5	0.97	1.0	1.0	1.1	1.1	1.2
a=5.5	b=0.5	1.5	1.5	1.5	1.6	1.6	1.6
a=7.5	b=0.5	1.9	1.9	1.9	1.9	2.0	2.0
a=15	b=3.7	3.8	3.8	3.8	3.8	3.8	3.8

3.6 Effect of Vertex z Resolution

As discussed above, a precise event vertex z position determination is very important for the discovery of Higgs in its $\gamma\gamma$ decay mode. The GEM central tracking system is designed to locate the event vertex with an accuracy of 1 mm in the z direction. However, with the standard luminosity of $\mathcal{L} = 10^{33}$ cm^{-2} s^{-1} and a bunch crossing frequency of 62.5 MHz, there are 1.6 minimum bias events (MBE) per bunch crossing, and the correct primary Higgs event vertex should be selected to achieve good mass resolution.

The selection of primary Higgs vertex with overlapping MBE's was studied by Yamamoto [12]. The algorithm follows an early study by L* [13], i.e. using the charged particle multiplicity coming out of each vertex in the event. The Monte Carlo programs used in simulation are PYTHIA 5.6 for Higgs signal and ISAJET 6.4.6 for the MBE's.

The vertex selection is done in two steps. In the first selection, all those vertices with good vertex position measurements are selected as the candidates. This cut is fairly arbitrary so long as the vertex location is well measured; and the loss of the Higgs signal is small. In this study it was required that a vertex should have at least

12 charged tracks with $p_t \geq 200$ MeV in $|\eta| \leq 2.5$. This selection keeps more than 98% of the Higgs signal, and the average number of MBE's is 1.43 per bunch crossing after this cut.

In the second selection, the vertex with the largest charged multiplicity is selected as the primary Higgs vertex. The cut used in selecting charged tracks is $p_t \geq 1$ GeV in $|\eta| \leq 2.5$. The study also shows that the result of the second selection is not sensitive to the cuts used in the first selection.

By using above two cuts, the probability of selecting the correct primary Higgs vertex is around 96%, which is not sensitive to the Higgs mass between 80 to 160 GeV. This probability is also not sensitive to the track reconstruction efficiency, provided that it is better than 80%.

Note, the production of MBE's has theoretical uncertainty. In this simulation ISAJET was used, since its phenomenalogical parametrization for the MBE's agrees well with the available hadron collider data. However, it is not sure that the center of mass energy dependence is correctly implemented in ISAJET. To evaluate the model ambiguity, MBE's were also generated by using PYTHIA program. The probability of selecting correct primary Higgs vertex is found to be around 85%, which is independent of Higgs mass between 80 to 160 GeV.

Figure 6 shows a distribution of charge multiplicity of Higgs events after $p_T > 1$ GeV and $|\eta| < 2.5$ cuts. Also shown in the figure are corresponding distributions of MBE's generated with PYTHIA and ISAJET programs.

Taking into account theoretical uncertainties, we conclude that the correct primary Higgs vertex can be determined with a better than 90% confidence. This indicates that 90% of the Higgs event will have a vertex z position resolution of 1 mm, while the other 10% of Higgs events will have vertex z resolution of 5 cm.

To be complete, Table 8 shows the ratio of $H \rightarrow \gamma\gamma$ peak width as function of the vertex z coordinate resolution (δz), energy resolution (a and b), assuming shower position resolution $\delta x = 1$ mm, for Higgs mass of 80 GeV. The numbers in this table are normalized to the case of a = 2 and b = 0.5. It is clear one must determine vertex z to a level of better than 5 mm so that the discovery potential of a high energy resolution EM Calorimeter is not compromised.

Table 8: Ratio of H→ $\gamma\gamma$ Peak Width as Function of δz, a and b

δz (mm)		1.0	2.0	3.0	5.0	10.	50.
a=2	b=0.5	1.0	1.0	1.1	1.1	1.5	5.4
a=5.5	b=0.5	1.5	1.5	1.6	1.6	1.9	5.5
a=7.5	b=0.5	1.9	1.9	1.9	2.0	2.2	5.6
a=15	b=1.0	3.8	3.8	3.8	3.8	3.9	6.5

4 Isolated Photon Background from QCD Jets

If there were no other background, the analysis for H→ $\gamma\gamma$ searches would have been finished in section 3. However, there are copious π^0's, and thus photons, produced in QCD jets. There are two major background from QCD jets: γ-jet and 2 jets final states. The production cross-section of γ-jet is 237 nb for $\hat{p}_T > 20$ GeV, including the following processes:

- qg→ γq: 226 nb; and
- qq→ γg: 11 nb.

The production cross section of QCD 2jets is 2 mb for $\hat{p}_T > 20$ GeV, including the following final states:

- gg: 1.54 mb;
- gq: 0.44 mb; and
- qq: 0.043 mb.

A narrow neutral jet consisting of multiple photons would fake an isolated photon. Single photons may also be produced in parton shower process. Figure 7 shows transverse energy distributions in EMC for two typical events from background processes: (a) γ-jet and (b) 2jets. To identify real photon and to reject QCD jet background, isolation cuts, shower shape analysis and preradiator may be used. The huge cross-section of these background processes make an accurate GEANT simulation not feasible in near future with foreseen computer power. It is thus crucial to use GEANT based

parametrization to obtain a realistic estimation of the background cross-section. In this section, the result of jet rejection cuts is presented in terms of QCD jet background cross-section in a mass range between 75 to 165 GeV.

It is interesting to note that at "parton" level[1] distributions of the invariant mass of $\gamma\gamma$, γ-jet and 2jets are similar at high mass end, as shown in Figure 8. After implementing the isolation cut described below, the energy vector of a fake isolated photon, in general, follows that of its parent parton. It is thus reasonable to assume that the $\gamma\gamma$ spectra from all three background processes have similar shape. Therefore, we need only to calculate γ/jet rejection ratio for a given rejection cut, and to deduce corresponding background cross-section for a given background process.

We further use relevant integrated cross-section, e.g. in a mass range between 75 and 165 GeV, to calculate total background cross-sections, and find significances for a given Higgs signal by scaling. Note, the shower shape and preradiator cuts described in this report do not change cross-sections of the Higgs signal and the irreducible $\gamma\gamma$ background very much, since the efficiency for single isolated photon passing these cuts are required to be larger than 90%.

4.1 Isolation Cut

The isolation cut uses the following procedure:

- Generate γ-jet or 2jets, use only jets within detector acceptance and with $E_T >$ 20 GeV. Deposit energies of complete events in calorimeter cells, as described in section 2. Mark cells which were hit by charged track in 8 kG field.
- Search through all cells to identify those cells hit by photons only, find E_T^{cell}.
- Charge Veto:

  Search through neighboring 8 cells, if any cell is hitted by a charged track or its E_T^{cell} is larger than that of the central cell $\Rightarrow$ **Reject**;
- Define the sum of E_T^{cell}'s of these 9 cells ($\sum_{9cells} E_T^{cell}$) as the E_T^{photon};
- Isolation Veto:

[1] We denote photon as one of the partons together with quarks and gluons.

if the sum of the transverse energies in a cone of radius R ($R=\sqrt{\Delta\eta^2+\Delta\phi^2}$), excluding the E_T^{photon}, is larger than 10% of the E_T^{photon} plus an isolation energy cut (E_T^{cut}):

$$\sum_{r<R} E_T - E_T^{photon} > (E_T^{cut} + 0.1E_T^{photon}) \Rightarrow \textbf{Reject.} \tag{7}$$

Table 9 shows the result of γ/jet isolation rejection ratios as function of the size of isolation cone (R) and the E_T^{cut}, for two QCD processes.

Table 9: Rejection Ratio (10^{-4})

Process	2jets			γ-jet		
E_T^{cut}	R=0.45	R=0.60	R=0.75	R=0.45	R=0.60	R=0.75
5 GeV	5.3	4.1	3.1	16	13	9.6
10 GeV	8.8	6.8	6.2	30	26	22
15 GeV	13	10	8.6	40	34	32
20 GeV	16	14	13	54	47	43

It is interesting to note that the rejection ratios from γ-jet and 2jets processes are different. This can be explained by different jet composition of these two processes. Since QCD 2jets have 12% quark jets and 88% gluon jets, while γ-jet have 95% quark jets and 5% gluon jets, we deduce that the isolation rejection ratio is about 10^{-3} for the quark jet and 2×10^{-4} for the gluon jet when the tightest isolation cut is used, i.e. 5 GeV E_T^{cut} in a 0.75 cone. We further attribute this factor of 5 difference in isolation rejection to:

- gluon jet is more broader than the quark jet in fragmentation; and
- gluon jet has lower probability of emitting a hard photon than a quark jet.

4.2 Further Rejection of Isolated Photon Candidate

The isolation cut along can not reduce the QCD jets background to below irreducible $\gamma\gamma$ background level. Looking at the isolated photon candidate (IPC) in details, however, one finds that many IPCs consist of more than one photons, and thus can be rejected by using shower shape analysis or preradiator. Figure 9 shows distributions of number

of photons in isolated photon candidates after an isolation cut of R = 0.75 and E_T^{cut} = 10 GeV for 100k events each of a) γ-jet and b) 2jets events.

A calculation was carried out to select IPCs passing a rough isolation cut: R = 0.45 and E_T^{cut} = 20 GeV. Events samples with one IPC from 2jets process and two IPCs from γ-jet process were recorded in data files on physics detector simulation facility (PDSF) disk at SSCL for further analysis.

To identify how close the IPCs are to a real photon, an energy weighted mean opening angle, $\bar{\theta}$, is calculated for each IPC:

$$\bar{\theta} = \frac{\sum_i E_i \theta_i}{\sum_i E_i} \tag{8}$$

where

$$\cos\theta_i = \frac{\vec{E}_i \cdot \vec{n}}{E_i}, \quad \vec{n} = \frac{\sum_i \vec{E}_i}{|\sum_i \vec{E}_i|}, \tag{9}$$

and $\vec{E}_i$ is the energy vector of the ith photon in the isolated photon candidate.

Figure 10 shows $\bar{\theta}$ distributions of isolated photon candidates after an isolation cut of R = 0.75 and E_T^{cut} = 10 GeV obtained from 100k events each of a) γ-jet and b) 2jets events. It is clear that those ICPs with a large $\bar{\theta}$ may be rejected by using shower shape analysis.

A detailed GEANT study by Yamamoto shows that in average, ICPs with $\bar{\theta} > 5$ mrad may be rejected by using a shower shape cut [14]. His analysis is based upon a fit on lateral shower profile in BaF_2 to an oval Gaussian distribution, and reject those ICPs with large minor. The simulation includes a rotation of all particles in IPCs, making $\vec{n}$ aiming at random at the full area of the central crystal. The vertex z position, where ICPs originated from, were smeared by 5 cm as a Gaussian. All particles in IPCs were shoot to an array consisting of 11 × 11 BaF_2 crystals. He then used a full GEANT simulation to deposit energies in BaF_2 crystals. An effective cut on minor of fitted oval, keeping more than 90% of real photons, was found to be consistent to $\bar{\theta} > 5$ mrad. Although the calculation was done for BaF_2 simulation, the same strategy can also be used for any fine segmented EMC, such as LAr accordion calorimeter.

Assuming that IPCs with $\bar{\theta} > 1$ mrad would be rejected by a preradiator, we can also estimate the corresponding background cross-sections after a preradiator cut. Several preradiator designs were proposed for GEM. See [14] for the details of a preradiator design for BaF_2.

As seen from Figure 9, there are single photons in IPCs which are originated

Table 10: QCD Background Cross-Sections (pb)

After Isolation						
Process	2jets			γ-jet		
E_T^{cut}	R=0.45	R=0.60	R=0.75	R=0.45	R=0.60	R=0.75
5 GeV	140	81	46	55	45	33
10 GeV	370	220	180	100	90	76
15 GeV	780	510	360	140	120	110
20 GeV	1200	940	800	190	160	150
After Shower Shape Analysis						
Process	2jets			γ-jet		
E_T^{cut}	R=0.45	R=0.60	R=0.75	R=0.45	R=0.60	R=0.75
5 GeV	73	34	20	31	26	21
10 GeV	160	120	89	54	50	42
15 GeV	250	210	140	68	59	57
20 GeV	310	260	230	83	73	66
After Preradiator						
Process	2jets			γ-jet		
E_T^{cut}	R=0.45	R=0.60	R=0.75	R=0.45	R=0.60	R=0.75
5 GeV	20	16	13	19	17	17
10 GeV	25	20	13	24	24	19
15 GeV	34	29	20	24	24	24
20 GeV	34	34	29	26	26	26
Bottom Line QCD Background						
Process	2jets			γ-jet		
E_T^{cut}	R=0.45	R=0.60	R=0.75	R=0.45	R=0.60	R=0.75
5 GeV	10	10	7.3	17	14	14
10 GeV	13	10	7.3	19	14	14
15 GeV	16	16	13	21	17	17
20 GeV	16	16	16	21	19	17

from QED process in parton shower. These single photons would provide a bottom line QCD jets background for $H \rightarrow \gamma\gamma$.

Table 10 summarises the result of the QCD background cross-sections as a function of the size of the isolation cone (R) and the E_T^{cut}. The cross-sections are calculated

in a $\gamma\gamma$ mass range between 75 and 165 GeV.

It is clear that a tightter isolation cut (large isolation cone and lower threshold) would provide more effective rejection, However, if R is too large or the threshold is too low, the signal acceptance would be hurt. The values applicable in analysis depends on detector performance, especially the sum of thermal and pile-up noise in a large cone. It should also be noticed that the study carried out in this report is a straightforward one. One may try more sophisticated isolation algorithms, e.g. using central tracker or part of calorimeter etc., to relax the requirements to the calorimeter noise. We discuss briefly two algorithms of this sort which use full calorimeter information.

An algorithm summing only cells in isolation cone with energy deposition larger than 3σ of noise was tested by author. Although less sensitive to the noise, this technique was found to provide a similar result to what presented in this report with some improvement. It is understood that when raising the energy threshold in each cell, the sensitivity to the associate jet energies in the isolation cone is also degraded. Another algorithm proposed by H. Ma [15] sums transverse energies in two cones with different size, both centred at IPC, and uses different E_T^{cut} threshold in these two cones. The result of this algorithm also improves rejection efficiency.

Assuming these improved algorithms are used, the corresponding E_T^{cut} threshold in a large cone can be lowered to 2.5 times the total noise without affect the acceptance of signals.

5 Misidentified Electron Background

In the last two sections we discussed backgrounds of real photon and fake isolated photons from QCD jets. Because of limited efficiency of central tracker, however, in a real detector an electron may also fake a photon if there is no charged track stub found at the front of the EM shower. A jet may fake an isolated electron and thus may also be recognised as an isolated photon.

The background against H$\rightarrow \gamma\gamma$ thus may be summarised as to have the following misidentification related contributions:

$$\begin{aligned}\sigma_{\text{"}\gamma\gamma\text{"}} &= \sigma_{ee}\, R^2(\gamma/e) + \sigma_{\gamma-jet}\,[R(\gamma/jet) + R(e/jet)R(\gamma/e)] + \\ &\quad \sigma_{2jets}\,[R^2(\gamma/jet) + 2R(e/jet)R(\gamma/e)R(\gamma/jet) + R^2(e/jet)R^2(\gamma/e)] \quad (10)\end{aligned}$$

where the first term is from a pair of isolated e^+e^-, such as Drell-Yan, the second term is from γ-jet final state, and the third term is from 2jets final state. R(e/jet) and R(γ/jet) are the probability of a jet faking an isolated electron and photon respectively, and R(γ/e) is the probability of misidentification of an isolated electron as an isolated photon.

5.1 Background from Isolated Electrons

The largest isolated e^+e^- background is Drell-Yan e^+e^- production, which has a production cross section of 2 nb. The event topology of Drell-Yan e^+e^- pair is very similar to H$\rightarrow \gamma\gamma$. If the overall detector design has no ability to distinguish γ versus electron, this background would seriously compromise H$\rightarrow \gamma\gamma$ measurement.

Figure 11 shows the invariant mass distribution of Drell-Yan e^+e^- after event selection cuts (dashed line). 41% of Drell-Yan e^+e^- events were accepted by the event selection cuts. The e^+e^- mass has a peak at Z^0 mass with a cross section of around 160 pb/GeV. As a comparison, the irreducible $\gamma\gamma$ background is also plotted in the figure, as a solid line. The $\gamma\gamma$ cross section at Z^0 mass is about 650 fb/GeV.

At the Z^0 peak, the Drell-Yan cross section is about 250 times larger than the irreducible $\gamma\gamma$ background. They are at the same level at the off resource tail when M(e^+e^-) is larger than 120 GeV. A detector, which has an R(γ/e) of less than 3%, would provide a 10^{-3} reduction to the Drell-Yan background. The Drell-Yan e^+e^- background after this reduction is also plotted in Figure 11 as a dotted histogram. It is clear that such an ability would not compromise the H$\rightarrow \gamma\gamma$ physics.

Note, a conventional tracker, such as L3 Time Expansion Chamber (TEC) at the front of BGO crystal calorimeter, may provide 2×10^{-4} rejection for $\gamma\gamma$ to Bhabha, which corresponds to 1.4% single track misidentification [11]. It is expected that GEM central tracker will provide an R(γ/e) of much less than ~3%. The Drell-Yan e^+e^- background thus is not a problem for H$\rightarrow \gamma\gamma$ detection.

The second largest isolated e^+e^- background is the e^+e^- pair production in the $t\bar{t}$ production. The electron pair in the $t\bar{t}$ is of the same size as the Drell-Yan background when M(e^+e^-) is larger than 110 GeV. A 3% rejection is more than enough to reduce it to a negligible level.

5.2 Jet Faking an Electrons

The probability of a QCD jet faking an isolated electron, R(e/jet), was studied by using the isolation strategy described in section 4.1 with an additional requirement of a charged track hitting the center cell.

Most of the isolated electron candidates (IEC) passing isolation cuts have a topology of overlapping energetic γ's with a low momentum charged track. To reduce these candidates, a very rough E-p matching is used:

$$|E_{Cal} - p_{track}| < 5\sqrt{\sigma_{Cal}^2 + \sigma_{track}^2} \tag{11}$$

where

$$\frac{\sigma_{Cal}}{E} = (\frac{10}{\sqrt{E}} \oplus 2)\%, \; and \; \frac{\sigma_{track}}{p^2} = 0.25\% \tag{12}$$

These energy resolution and momentum resolution are very conservative. More conservative cut

$$\frac{p_{track}}{E_{Cal}} \leq 0.5 \tag{13}$$

works equally well.

All the candidates which pass these two cuts contain real electrons accompanying no γ or a few low momentum γ's. The total electron candidate which passes these cuts were 6 among 300k 2jets events, and 2 among 300k γ-jet events. In these samples, all IECs are from heavy quark decays (c, b and t), and when tightter cuts are applied, only decays from b and t quarks remained.

Table 11 lists the result of the calculation by using E_T^{cut} = 5 GeV and three cone size R = 0.3, 0.45 and 0.6. 300k events each for 2jets and γ-jet final states were

generated in this calculation. Also shown in the table is R(e/jet) after E-p matching and final cross sections of "γ-e" and "e-e" configurations.

Table 11: Probability of a Jet Faking an Isolated Electron

	2jets			γ-jet		
R	0.30	0.45	0.60	0.30	0.45	0.60
R(e/jet) by isolation (10^{-5})	21	12	8.1	22	12	9.8
R(e/jet) by E-p match (10^{-5})	5.6	4.0	0.7	3.7	3.7	3.7
R(γ/jet) by isolation (10^{-4})	7.4	5.3	4.1	21	16	13
"γ-e" (pb)	22	11	1.5	1.3	1.3	1.3
"e-e" (pb)	0.8	0.4	0.01			

The probability of a jet faking an isolated electron, R(e/jet), can be compared to the probability of a jet faking an isolated photon, R(γ/jet) as listed in Table 9. It is interesting to note that

- contrary to the case of faking a photon, both gluon jet and quark jet have a similar probability of faking an isolated electron; and
- R(e/jet) is more than 10 times smaller than R(γ/jet).

The consequence of fake isolated electrons to H$\rightarrow \gamma\gamma$ detection can be observed from the last two lines of Table 11, where background cross sections of "γ-e" and "e-e" are listed. These cross sections are negligible, compared to the irreducible $\gamma\gamma$ background cross section of 43 pb for $M_{\gamma\gamma} > 75$ GeV, taking into account the R(γ/e) of 3%.

6 H$\rightarrow \gamma\gamma$ for two GEM Calorimeter Systems

As discussed in previous two sections, the sum of thermal and pile-up noise in an isolation cone would affect the implementation of a tight isolation cut. The application of the isolation cut for two calorimeter systems proposed by GEM collaboration is described below.

- BaF_2 followed by a scintillation calorimeter:

  Since both BaF_2 and scintillation calorimeter have low thermal noise. The dominant contribution to the noise in a large area is the pile-up noise, which depends on integration time and luminosity. Assuming running at a standard luminosity, this system would provide around 2 GeV noise in a 0.75 isolation cone, i.e. R = 0.75 and E_T^{cut} = 5 GeV can be used.

- Liquid Argon calorimeter:

  The design of LAr system was optimised so that the thermal and pile-up noise contributions are roughly equal in a trigger tower [16]. This system has 4 GeV noise in a 0.6 isolation cone, i.e. R = 0.6 and E_T^{cut} = 10 GeV can be used.

Following the above assumption, we calculate the total background cross-section from $\gamma\gamma$, γ-jet and 2jets processes by using the isolation cut, shower shape analysis and preradiator, as discussed in section 4. The bottom line QCD background cross-section is also calculated. Table 12 lists the total background cross-sections. Also listed in the table are the background scaling factor (B.F.) which is the total background cross-section normalized to the irreducible $\gamma\gamma$ background of 31 pb for the BaF_2 calorimeter. Note, the BaF_2 and LAr have different background cross-section because of different isolation cut used. The same difference also shows up in accepted signal cross-section.

Assuming that the shape of $\gamma\gamma$ invariant mass spectra from all background sources is the same, total background spectrum may be obtained by scaling the irreducible $\gamma\gamma$ background with a factor of B.F. Figure 12 shows spectra of Higgs signals of 80, 100, 120, 140 and 160 GeV superimposed on total background after (a) shower shape analysis and (c) preradiator rejection for BaF_2 calorimeter. The corresponding background subtracted spectra are shown in Figure 12b) and d). The significance of these signals in one SSCY is 3.0, 5.7, 9.2, 10 and 3.9 after shower shape analysis and 3.3, 6.1, 9.9, 11 and 4.9 after preradiator rejection.

Table 12: Total Background Cross-Section (pb)

	BaF_2 System					LAr System				
Process	$\gamma\gamma$	γ-jet	2jets	Total	B.F.	$\gamma\gamma$	γ-jet	2jets	Total	B.F.
Isol.	31	33	46	110	3.5	34	90	220	344	11
S.S.	31	21	20	72	2.3	34	50	120	204	6.6
P.R.	31	17	13	61	2.0	34	24	20	78	2.5
Irr.	31	14	7.3	52	1.7	34	14	10	58	1.9

The same spectra are shown in Figure 13 for the LAr option. The significance in one SSCY is 1.3, 2.8, 4.7, 5.1 and 2.0 after shower shape analysis, and 2.3, 4.4, 7.6, 8.2 and 3.3 after preradiator rejection.

Note, the event numbers listed in Figures 12 and 13 are for a perfect EMC without including the acceptance loss discussed in section 2.2. Taking into account the relative acceptance listed in Table 3, the numbers of both signal and background events should be reduced to 73% and 69% respectively for BaF_2 calorimeter and LAr calorimeters. The corresponding significance should be reduced to 85% and 83% respectively.

Taking into account high order QCD corrections to the Higgs production [9], i.e. the K factor of 1.5, the corresponding numbers of signal events and significance should both be increased by a factor of 1.5. Note, the dominant irreducible background process of $gg \rightarrow \gamma\gamma$ is an $O(\alpha_s^2)$ process.

7 $H(t\bar{t}/W) \rightarrow \gamma\gamma\ell X$ Searches

Both $Ht\bar{t} \rightarrow \gamma\gamma\ell X$ and $HW \rightarrow \gamma\gamma\ell X$ are complementary channels can be used to cover the Higgs mass range below 140 GeV [17]. As shown in Figure 2, the signal cross-section of sum of these two channels is in an order of few fb. However, with a lepton (ℓ) tagging the irreducible background for $H \rightarrow \gamma\gamma$ can be eliminated. The $\gamma\gamma$ invariant mass spectrum of these two processes thus has much less background.

In this section we discuss searches for intermediate mass Higgs boson by using these two channels. Since we are looking for $\gamma\gamma$ invariant mass to locate Higgs signal, most elaboration on effect of detector resolutions to the Higgs peak width discussed in section 3 is also applicable to this search. The main differences are:

- with an associate charged lepton in final state and the fine resolution of its impact parameter, the Higgs vertex determination would be more accurate;
- the statistics of both signal and background is low, so that the effect of high resolution is not directly correlated to the discovery time, as shown in Equation 5. The consequence of $\gamma\gamma$ mass resolution to the significance will be discussed in section 7.2.

7.1 Signal and Background

The main backgrounds against $H(t\bar{t}/W) \rightarrow \gamma\gamma\ell X$ searches are:

- $t\bar{t}\gamma\gamma$: 80 fb;
- $b\bar{b}\gamma\gamma$: 2 pb;
- $W\gamma\gamma$: 23 fb;
- $t\bar{t}$: 16 nb.

A combination of Monte Carlo programs is used to simulate the first three backgrounds. The hard scattering processes are generated by using PAPAGENO 3.6 [18]. The initial and final state parton radiation, hadronization and decays are generated by using PYTHIA 5.6 [4].

The $t\bar{t}$ background was generated with PYTHIA 5.5 program. The study was done with 2.6M events. It is interesting to note that the isolation cut along can not

reduce $t\bar{t}$ background to a negligible level. With a lepton tagging, the $t\bar{t}$ final state has 4 quark jets. According to Table 9, an effective isolation cut can achieve 1.3×10^{-3} rejection for $E_T^{cut} = 5$ GeV and R = 0.6. Together with a combinatory factor of 6, the isolation would provide a rejection of 10^{-5}, which leads to a background cross-section of $t\bar{t} \rightarrow \ell X$ of 90 fb, or 50 to 80 times higher than the $Ht\bar{t} \rightarrow \gamma\gamma\ell X$ signal.

Since the $\gamma\gamma$ invariant mass distribution obtained from IPCs from $t\bar{t}$ process was spread out, a cut on interesting mass interval between 75 and 165 GeV would reduce the background by a factor of 3. It was also found that the two photon system from signal has a large p_T than that from background. A cut on joint p_T of $\gamma\gamma$ system in an order of 40 GeV would effectively reduce background by another factor of 3. It is also interesting to note that while a larger cone helps in rejecting quark jet background, the best cone size for lepton isolation is 0.3, which helps to maintain high signal acceptance.

Table 13: Numbers of Signal and Background Events in One SSCY

	p_t^{cut} = 20 GeV			p_t^{cut} = 40 GeV		
R	0.30	0.45	0.60	0.30	0.45	0.60
Higgs (80GeV)	28	23	18	21	18	14
Higgs (90GeV)	30	25	20	24	20	17
Higgs (100GeV)	30	25	21	25	21	17
Higgs (120GeV)	24	20	16	22	18	15
Higgs (140GeV)	17	15	13	15	14	11
Higgs (150GeV)	10	8	7	9	8	6.5
Higgs (160GeV)	4	3.4	2.7	3.6	3	2.5
$t\bar{t}\gamma\gamma$ (75-165 GeV)	55	46	32	51	42	30
$W\gamma\gamma$ (75-165 GeV)	32	31	30	21	21	20
$t\bar{t}$ (75-165 GeV)	308	246	185	123	61	61

The following cuts are therefore used in our $Ht\bar{t} \rightarrow \gamma\gamma\ell X$ searches:

- $|\eta_\ell| < 2.5$, $P_T^\ell > 20$ GeV, R = 0.3;
- $|\eta_\gamma| < 2.5$, $P_T^\gamma > 20$ GeV, R = 0.3, 0.45 or 0.6;

- isolation cut $\Rightarrow$ reject $t\bar{t}$:

$$\sum_{r<R} E_T - E_T^{photon} < 5GeV + 0.1E_T^{photon}$$

- p_T of di-photon $> p_T^{cut} \Rightarrow$ reject $t\bar{t}$;
- Shower Shape Analysis: $\bar{\theta} < 5$ mrad, as dicussed in section 4.

Signal and background events after these cuts are listed in Table 13.

The $b\bar{b}\gamma\gamma$ background is rejected by the isolation cut to a negligible level. It is clear from this table, that the largest background is the fake $\gamma - \gamma$ pairs from $t\bar{t}$ production, and p_T^{cut} applied to joint momentum of $\gamma - \gamma$ pair is an effective cut to eliminate this background.

Figure 14 shows $\gamma\gamma$ invariant mass spectra collected in one SSCY with Higgs signals of 80, 100, 120, 140 and 160 GeV superimposed over a sum of all backgrounds for three energy resolutions: (a) $(2/\sqrt{E} \oplus 0.5)\%$; (b) $(7/\sqrt{E} \oplus 0.5)\%$; and (c) $(15/\sqrt{E} \oplus 1)\%$. The cuts used are R = 0.45 and $p_T^{cut} = 40$ GeV.

Note, the event numbers shown in Table 13 and Figure 14 are for a perfect EMC without including the acceptance loss discussed in section 2.2. Taking into account of the relative acceptance listed in Table 3, the numbers of both signal and background events should be reduced to 62% and 56% respectively for BaF_2 calorimeter and LAr calorimeters.

7.2 Significance

Since the statistics of both signal and background is low, Equation 5 can not be used to estimete the significance. We thus estimate the significance by using two methods: one is pure mathematical calculation based upon a convolution of two Poisson probability distributions, and the other is a Monte Carlo method by trying the experiment many times. The result of these two methods are consistent. In this section, we describe these two methods and their result on significance.

7.3 Mathematical Method

We assume a signal peak with defined width is observed over some background, and both process have low statistics. The expected number of signal events in mass interval

of $M_H \pm \sigma_{\gamma\gamma}$ is N_s, and the corresponding number of background events is N_B. The probability of observing certain number of events (n) follows a Poisson statistics:

$$P_n(\lambda) = \frac{\lambda^n e^{-\lambda}}{n!} \tag{14}$$

where λ is the expected value, i.e. N_S for the signal and N_B for the background.

If one observe n events, the probability of these events caused by background fluctruation is:

$$Prob = \sum_{m=n}^{\infty} P_m(N_B) \tag{15}$$

Taking into account the fluctruation of observed events which has an expectation value of $N_B + N_S$, the final probability of observing a signal which is caused by background fluctuation is:

$$Prob = \sum_{n=0}^{\infty}[P_n(N_B + N_S] \times \sum_{m=n}^{\infty} P_m(N_B)] \tag{16}$$

This probability can be converted to the significance in terms of standard deviation (σ) defined from a Gaussian distribution, e.g. a Prob = 0.0027 is mapped to 3σ, and 0.000057 is 5σ etc. It is interesting to note, when the expected number of background events is high, Equation 16 corresponds to the significance defind in Equation 5.

Table 14: Siginicance of $H(t\bar{t}/W) \rightarrow \gamma\gamma\ell X$ Search for Three Energy Resolutions

$\Delta E/E$ (%)			$2/\sqrt{E} \oplus 0.5$		$7.5/\sqrt{E} \oplus 0.5$		$15/\sqrt{E} \oplus 1.0$	
M_H (GeV)	$\sigma_{\ell\gamma\gamma}$ (fb)	N_S	$\sigma_{M_{\gamma\gamma}}$ (GeV)	S	$\sigma_{M_{\gamma\gamma}}$ (GeV)	S	$\sigma_{M_{\gamma\gamma}}$ (GeV)	S
80	8.4	12	0.34	3.5/3.2	0.66	3.2/2.8	1.3	2.9/2.3
90	8.0	14	0.37	3.9/3.5	0.70	3.5/3.1	1.4	3.1/2.6
100	7.8	14	0.40	3.9/3.5	0.73	3.5/3.1	1.45	3.1/2.6
120	6.9	13	0.45	3.7/3.3	0.77	3.4/3.0	1.5	3.0/2.5
140	4.2	9	0.53	3.0/2.7	0.89	2.7/2.4	1.7	2.4/2.0
150	2.6	5.4	0.58	2.0/1.8	0.95	1.8/1.5	1.9	1.5/1.2

Table 7.3 lists significance calculated according to Equation 16 for $H(t\bar{t}/W) \rightarrow \gamma\gamma\ell X$ searches with three energy resolutions in one SSCY. In the table, the two numbers for the significance are the ones using the expected and double of the expected number of backgrounds.

Figure 15 shows the significance of this search as a function of SSCY calculated for three energy resolutions and 6 different Higgs masses. The up bound of the band corresponds to the calculated background, while the low bound of the band corresponds to the background scaled by a factor of two. It is clear that high resolution also corresponds to a short discovery

7.4 Monte Carlo Method

In the second method, signals and backgrounds are generated bin-by-bin using Poission statistics to simulate one experiment, and the distribution is fit using Likelyhood method by Minuit with a smooth background and a Gaussian to find the area (A) and the error of the area (δA) of the signal. The significance of the signal in this experiment is then defined as $A/\delta A$.

When the event and background rate is low, this significance varies from one experiment to another, and this value itself is not so meaningful. A more meaningful significance, $S_{2/3}$, is defined as the significance that 2 out of 3 experiments, one will observe at least this significance. E.g., $S_{2/3} = 5$ means the probability that one will observe 5σ effect is over 67%, or if one does the same experiment 3 times, one will observe 5σ effect in 2 experiments. Monte Carlo events are used to generate many sets of experiments to find $S_{2/3}$.

The estimation of rare backgrounds are very difficult, because of the incompleteness of the theory, Monte Carlo implementation and the detector simulation. To estimate these uncertainties and the robustness of the experiment, the significance was also calculated using the background with twice as much as the current estimation.

8 H→ZZ/ZZ* →$e^+e^-e^+e^-$ Searches

As shown in Table 4 and Figure 2, for Higgs mass above 130 GeV considerable Higgs would decay to 4 electrons through ZZ/ZZ* decay, where Z* denotes a virtual Z. The signal in this search has a distinguished feature of four isolated electrons, and has a cross section of few fb.

It is known that requiring four isolated leptons would reduce all QCD jet background to a negligible level. There are, however, irreducible ZZ/ZZ* background and $Zq\bar{q}$ (q is a heavy quark b or t) background. Both may provide four isolated electrons. The cross section of these two backgrounds are:

- $q\bar{q}/gg \rightarrow ZZ/ZZ^* \rightarrow e^+e^-e^+e^-$: 24 fb;
- $Zt\bar{t} \rightarrow e^+e^-e^+e^-X$:
- $Zb\bar{b} \rightarrow e^+e^-e^+e^-X$:

The following cuts were used in this serach:

- $|\eta_\ell| < 2.5$;
- $E_{T_\ell} > 5$ GeV;
- Isolation: $\Sigma_{R=0.3} E_T - E_{T_\ell} < 5GeV + 0.1 E_{T_\ell} \Rightarrow$ reduce Decay from Heavy Quarks.
- $|M_{\ell^+\ell^-} - M_z| < 2$ GeV $\Rightarrow$ suppress γ^*;
- In the case of Z*, require one pair mass:

  10 GeV $< M_{\ell^+\ell^-} < M_z + 2$ GeV

add table and figures.

Similar to Table 6, Table 15 shows the ratio of of H→$e^+e^-e^+e^-$ peak width as function of a and b, normalized to the BaF_2 crystal calorimeter resolution: $2\%/\sqrt{E} \oplus 0.5\%$, for Higgs mass of 140 GeV and 170 GeV.

Table 15: Ratio of $H \rightarrow e^+e^-e^+e^-$ Peak Width as Function of a and b

a	2.0	3.0	5.5	7.5	10	15
M_H = 140 GeV						
b=0.5	1.0	1.1	1.6	2.0	2.5	3.7
b=1.0	1.8	1.9	2.1	2.5	3.0	4.0
b=1.5	2.6	2.7	2.9	3.1	3.5	4.3
b=2.0	3.4	3.5	3.7	3.9	4.4	5.0
M_H = 170 GeV						
b=0.5	1.0	1.0	1.2	1.6	2.0	3.0
b=1.0	1.5	1.6	1.8	2.0	2.3	3.2
b=1.5	2.1	2.2	2.3	2.6	2.7	3.3
b=2.0	2.7	2.8	3.0	3.1	3.4	4.1

References

[1] GEM Collaboration, Letter of Intent to the SSCL, November 30, 1991.

[2] CERN Green Book, *"ECFA Workshop on LEP 200"*, Aachen, September, 1986.

[3] R.Y. Zhu, GEM Internal note **GEM TN-91-32**, November 30, 1991.

[4] H. Benson and T. Sjostrand, *"A Manual to the Lund Monte Carlo for Hadronic Processes"*, PYTHIA version 5.6, September, 1991.

[5] R.Y. Zhu, GEM Internal note **GEM TN-92-48 Rev A.**, January 18, 1992.

[6] M. Seman, Talk given in GEM Council Meeting, June 4, 1992.

[7] L3 Collaboration, *Nucl. Instr. and Meth.* **A289** (1990) 35.

[8] R.Y. Zhu, Proceedings of ECFA LHC Workshop, Aachen, October 1990, Volume III p. 411.

[9] A. Djouadi, M. Spira and P. M. Zerwas, Phys. Lett. **B264** (1991) 440.

[10] D. Dicus and S. Willenbrock, Phys. Rev. **D37** (1988) 1801.

[11] Y. Karyotakis *et al.*, Final State Photons, L3 Internal Note, February 1992.

[12] H. Yamamoto, GEM Internal note GEM-TN-92-??.

[13] L* Collaboration, Report to the PAC, July 7, 1990.

[14] H. Yamamoto, GEM Internal note GEM-TN-91-33.

[15] H. Ma, GEM Internal note.

[16] BNL Report, **BNL 52244**, Ed. B.Yu and V. Radeka.

[17] W.J. Marciano and F. Paige, BNL Preprint, **BNL-45805**
J.F. Gunion *et al.*, SDC report, **SDC-91-00057**
R. Kleiss *et al.*, Phys. Let. **B253** (1991) 269;
Z. Kunszt *et al.*, Phys. Let. **B271** (1991) 247.

[18] I. Hinchliffe, A Monte Carlo Parton Generator, unpublished.

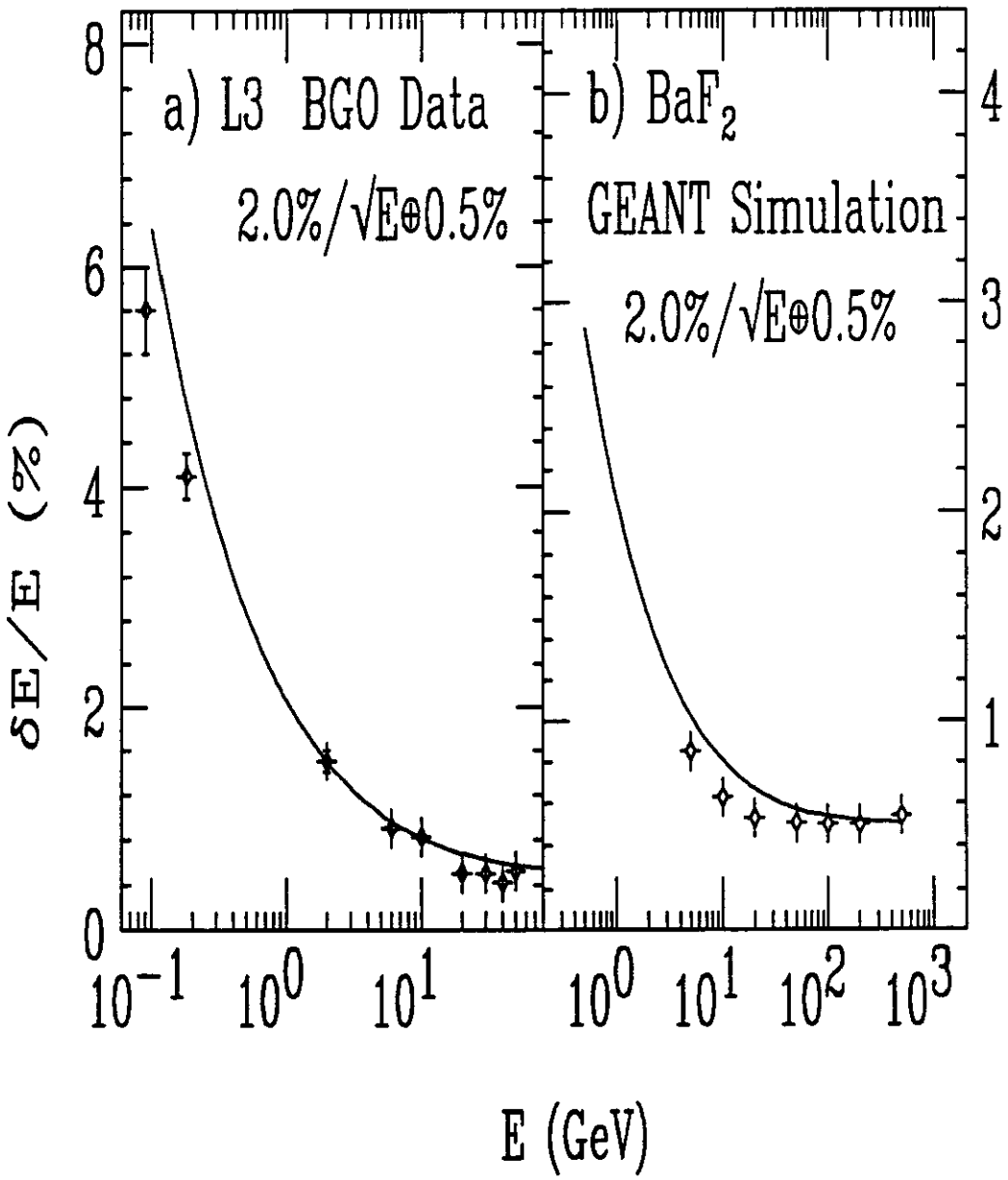

Figure 1: Energy Resolutions of (a) L3 BGO calorimeter, measured at CERN test beams with 4000 crystals, and (b) BaF_2 calorimeter, calculated with GEANT simulation. The solid curves represent a simple parametrization of $2\%/\sqrt{E} \oplus 0.5\%$.

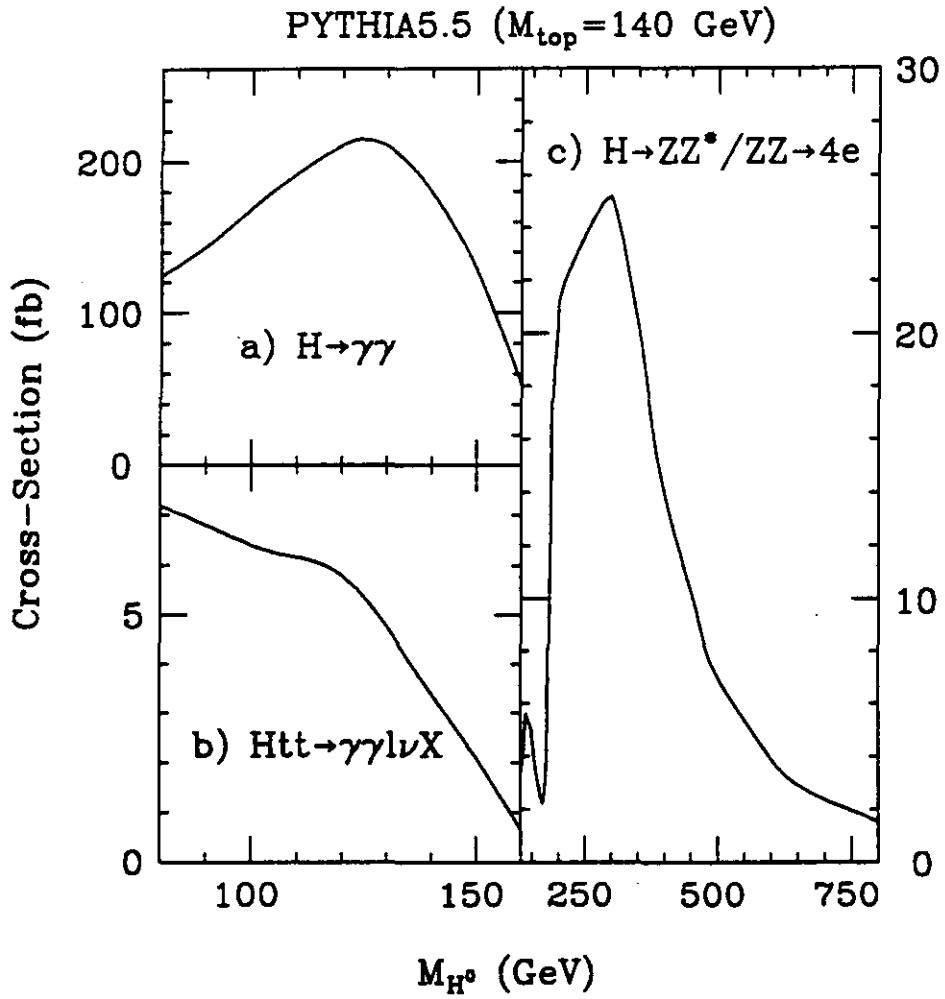

Figure 3: Cross-sections of $H^0 \rightarrow \gamma\gamma$ (a), $Ht\bar{t} \rightarrow \ell\gamma\gamma$ (b) and $H^0 \rightarrow ZZ^*/ZZ \rightarrow e^+e^-e^+e^-$ (c) events at the SSC are shown as functions of Higgs mass.

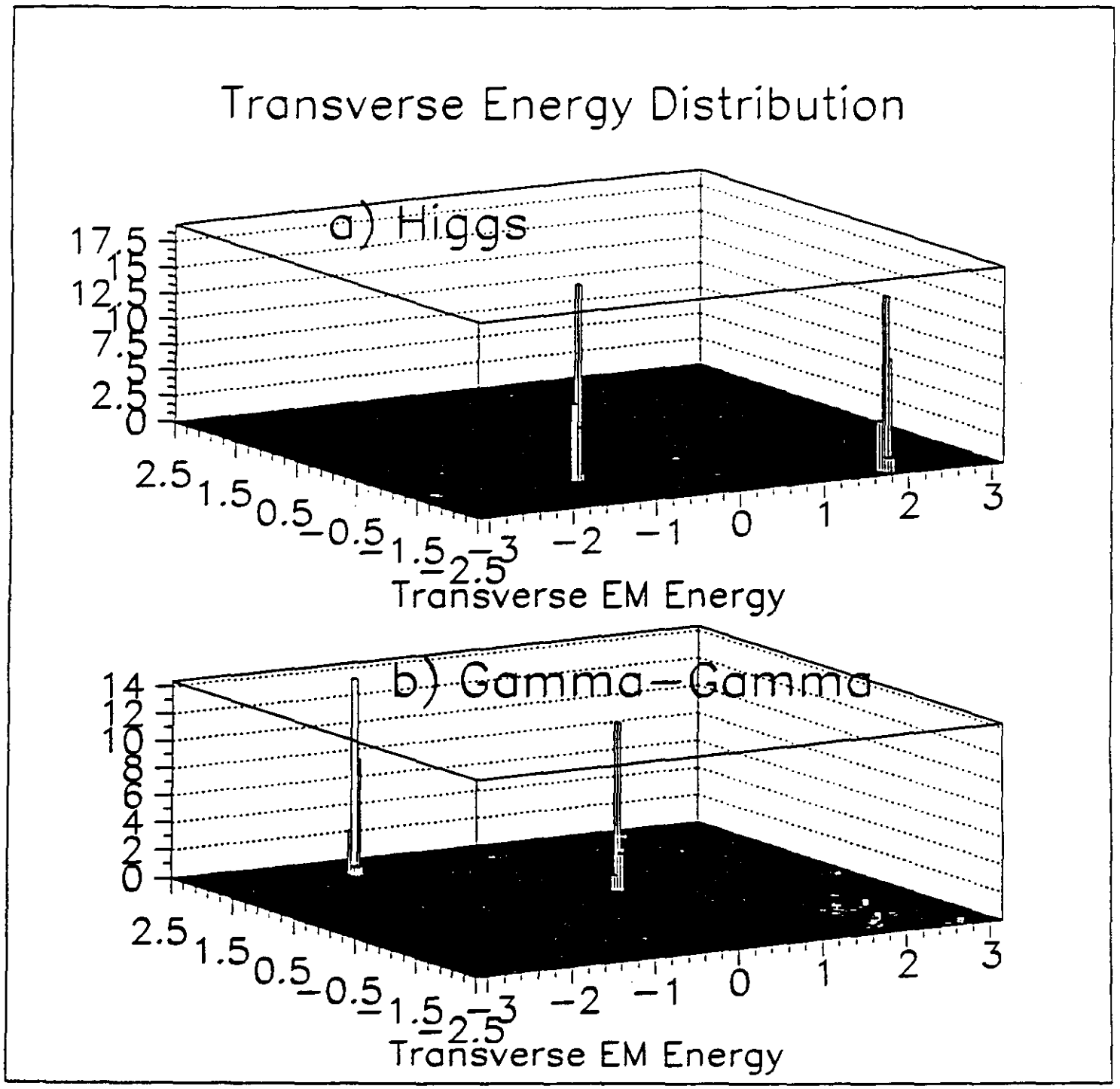

Figure 3: Transverse energy distributions in EMC for two typical events from signal process of H→ $\gamma\gamma$ (a) and irreducible background process $\gamma\gamma$ (b).

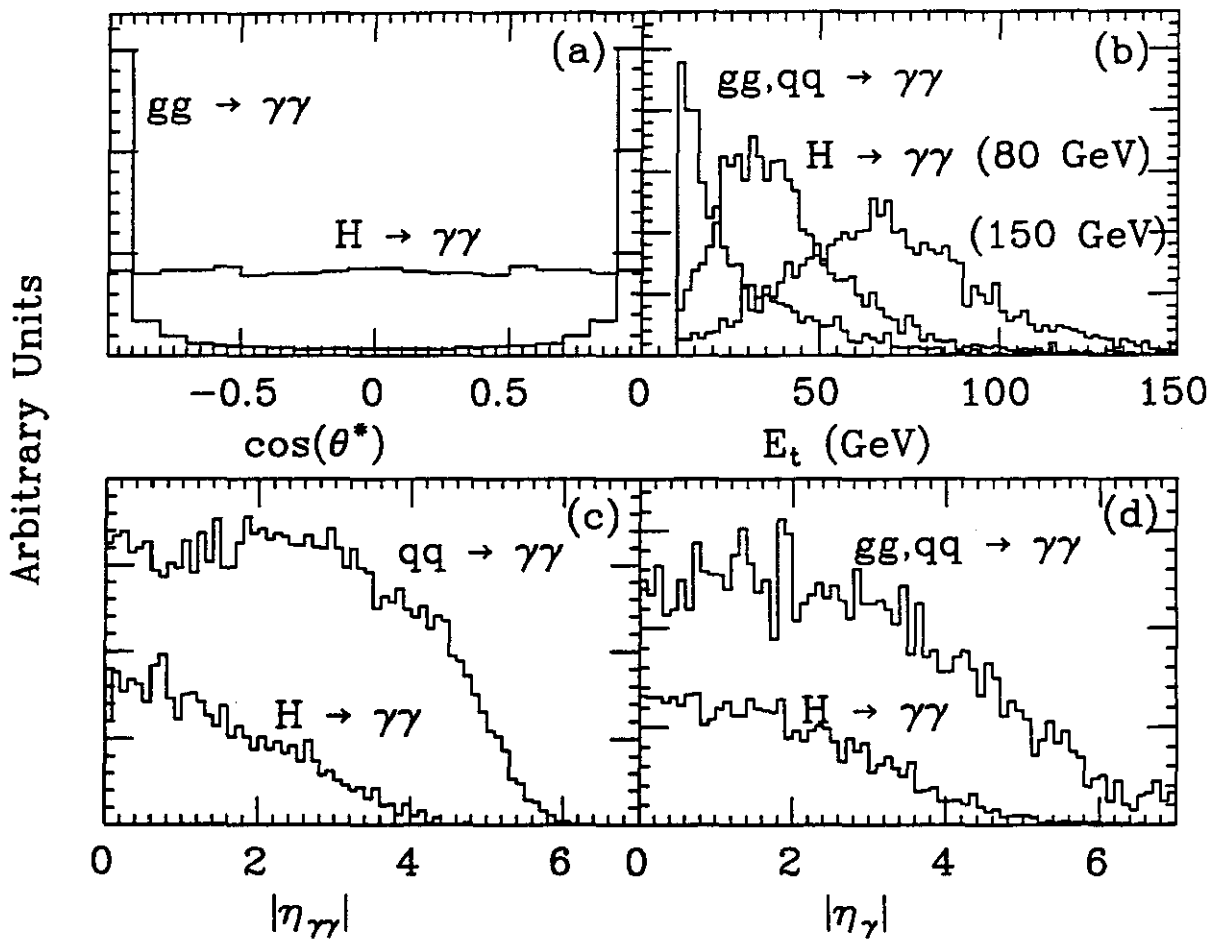

Figure 4: Compariosn of distributions between H→ $\gamma\gamma$ and irreducible background: (a) $\cos\theta^*_\gamma$, (b) E^γ_T, (c) $|\eta_{\gamma\gamma}|$; and (d) $|\eta_\gamma|$.

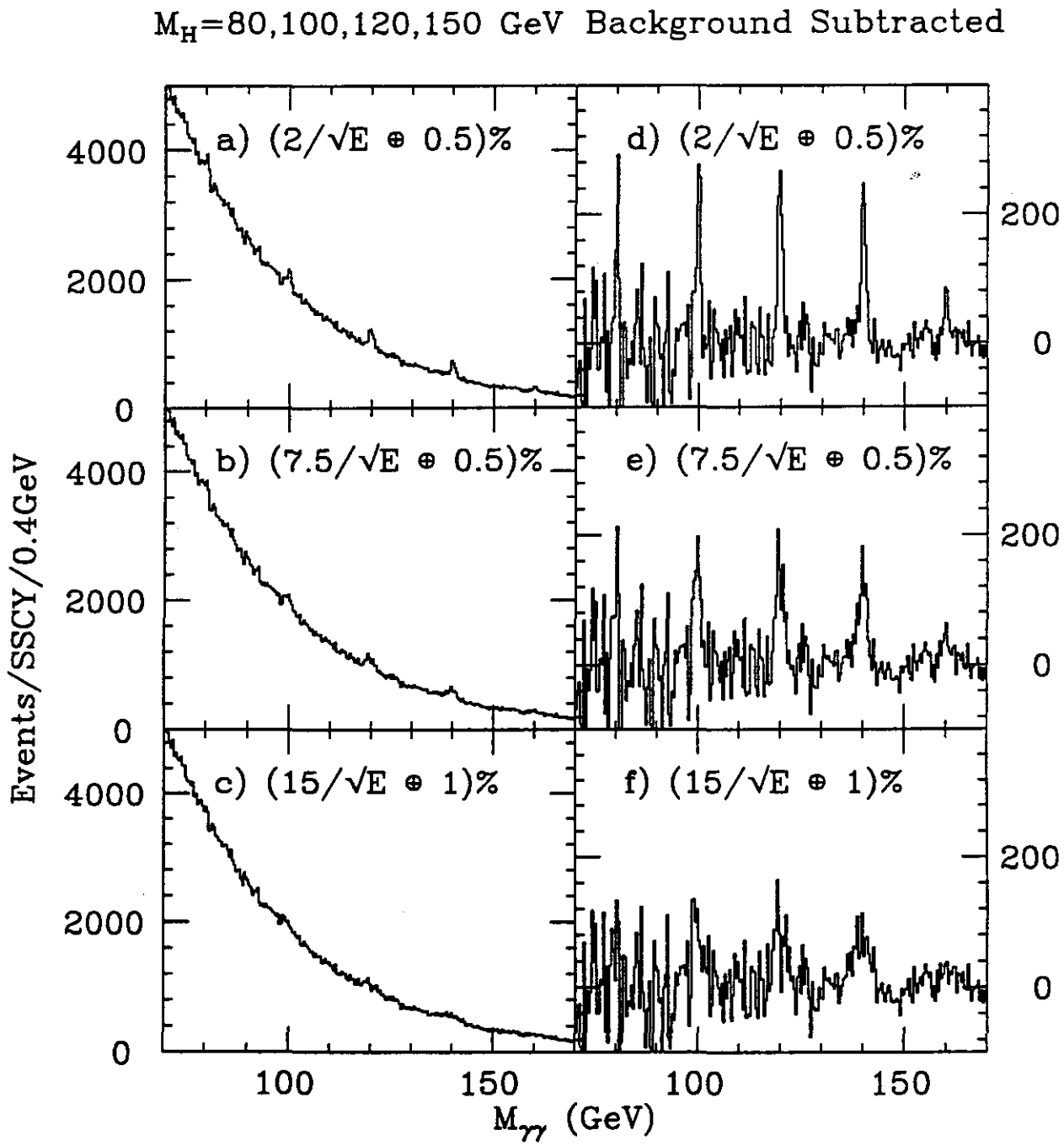

Figure 5: $\gamma\gamma$ invariant mass spectra obtained within 1 SSCY with H$\rightarrow$ $\gamma\gamma$ signals of 80, 100, 120, 140 and 160 GeV, superimposed on irreducible background are shown for three energy resolutions: (a) $(2/\sqrt{E} \oplus 0.5)\%$; (b) $(7.5/\sqrt{E} \oplus 0.5)\%$; and (c) $(15/\sqrt{E} \oplus 1.0)\%$. Corresponding background subtracted spectra are shown in (d), (e) and (f).

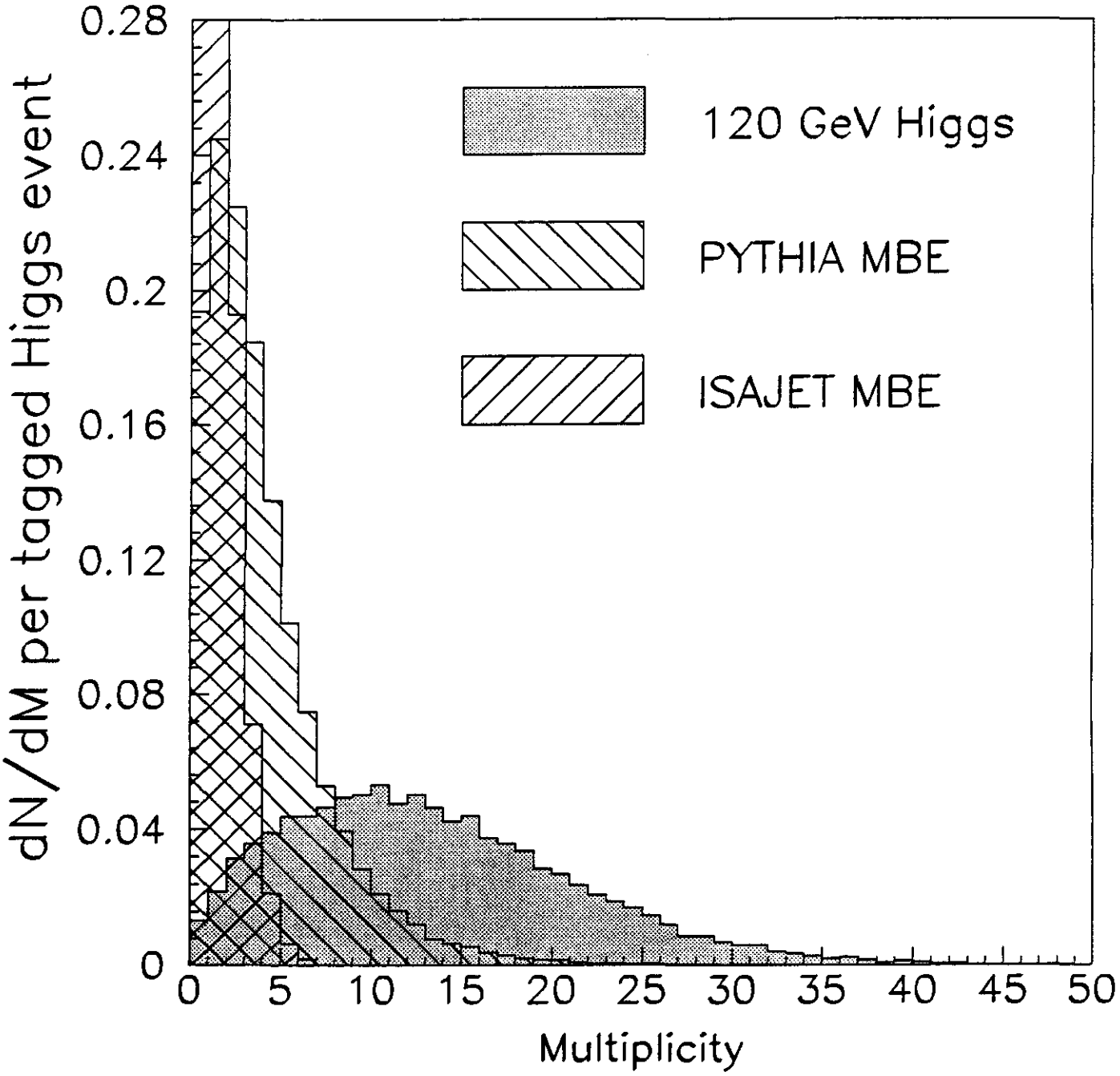

Figure 6: Charge multiplicity distributions after $p_T > 1$ GeV and $|\eta| < 2.5$ cuts for a 120 GeV Higgs signal and minimum bias events backgrounds generated by using PYTHIA and ISAJET programs.

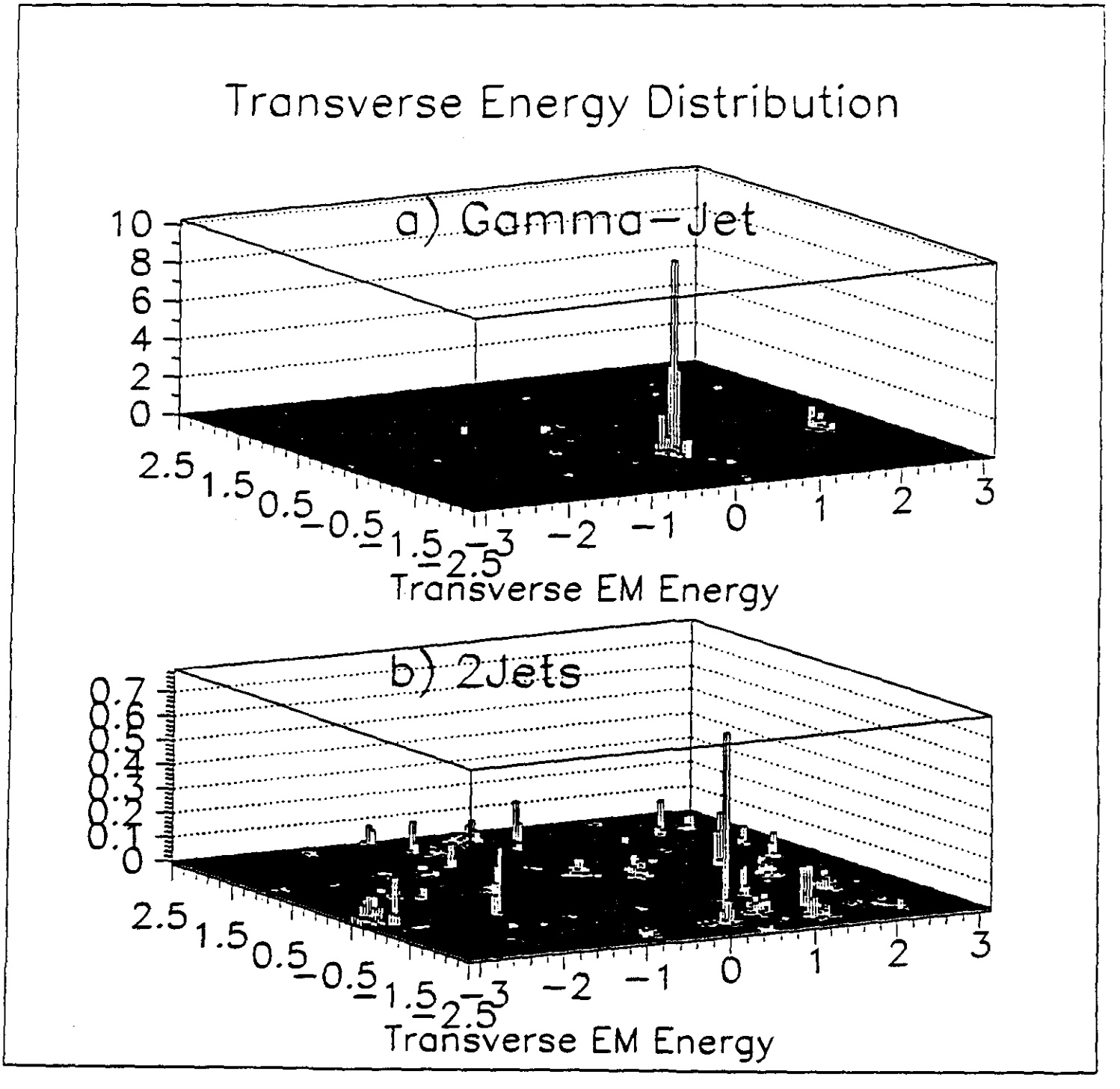

Figure 7: Transverse energy distributions in EMC for two typical events from background processes: (a) γ-jet and (b) 2jets.

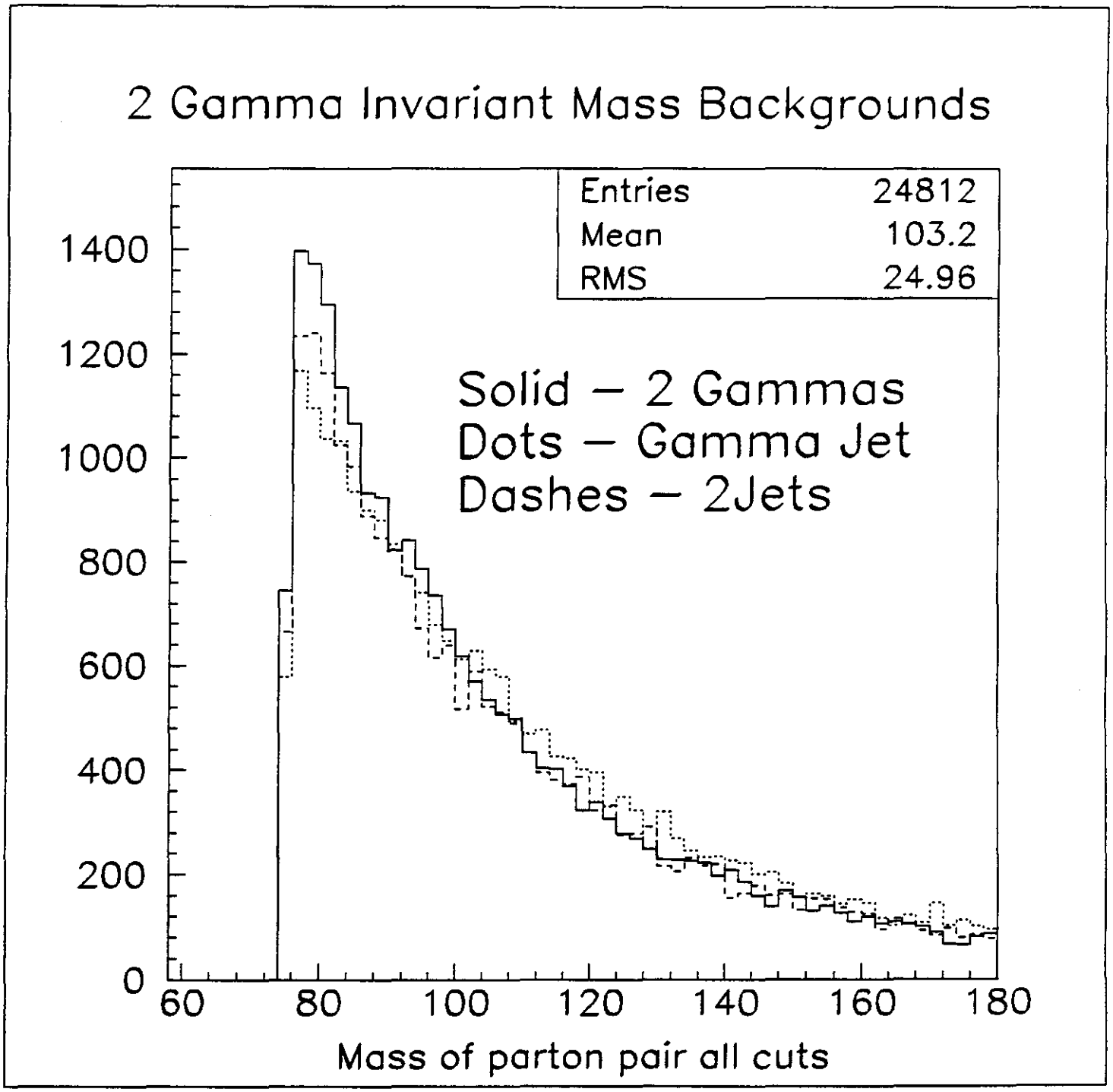

Figure 8: Comparison of parton invariant mass spectra from three QCD processes: $\gamma\gamma$, γ-jet and 2jets.

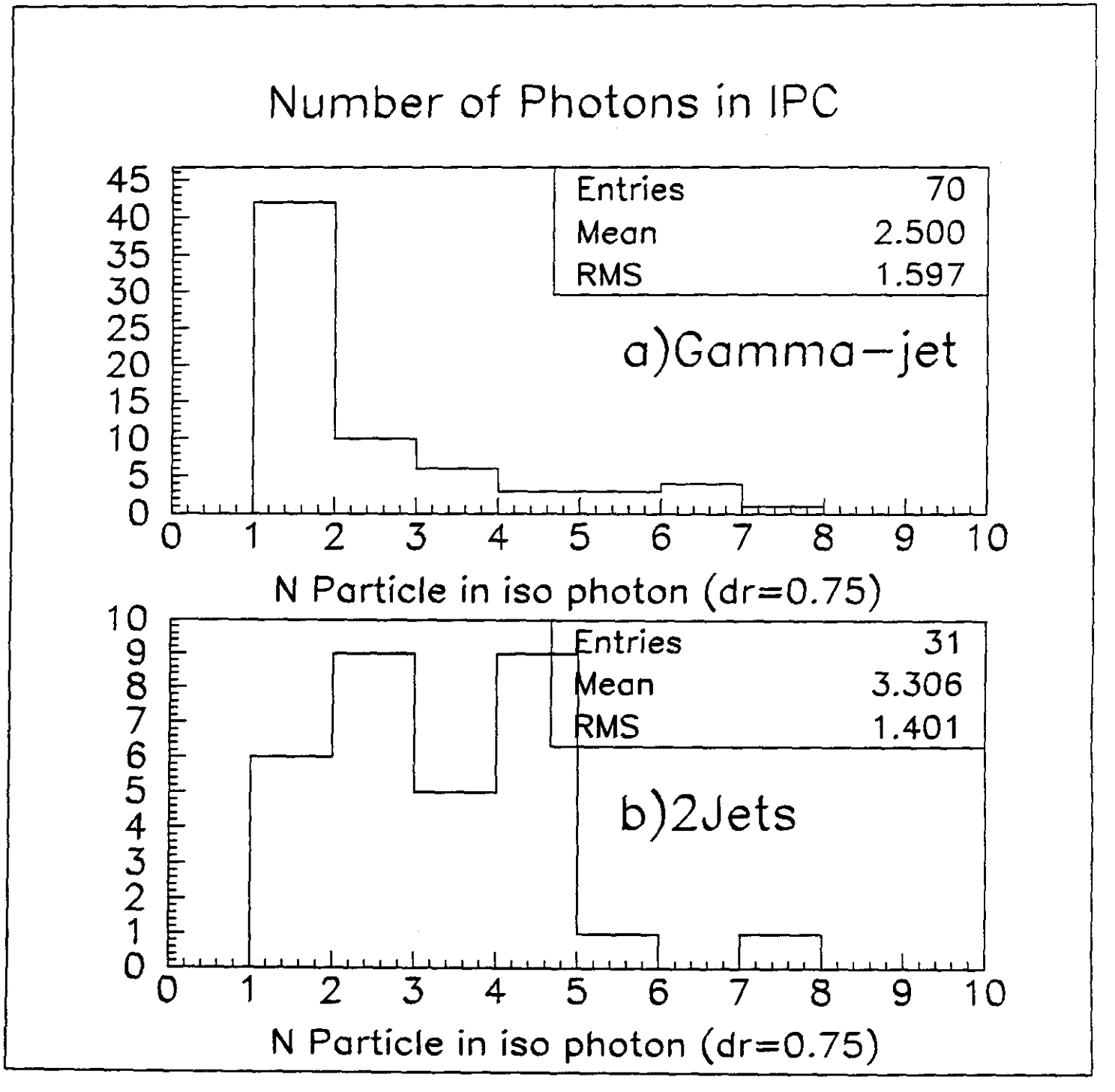

Figure 9: Distributions of photon numbers in isolated photon candidates, passing an isolation cut of R = 0.75 and E_T^{cut} = 10 GeV from 100k events each of (a) γ-jet and (b) 2jets.

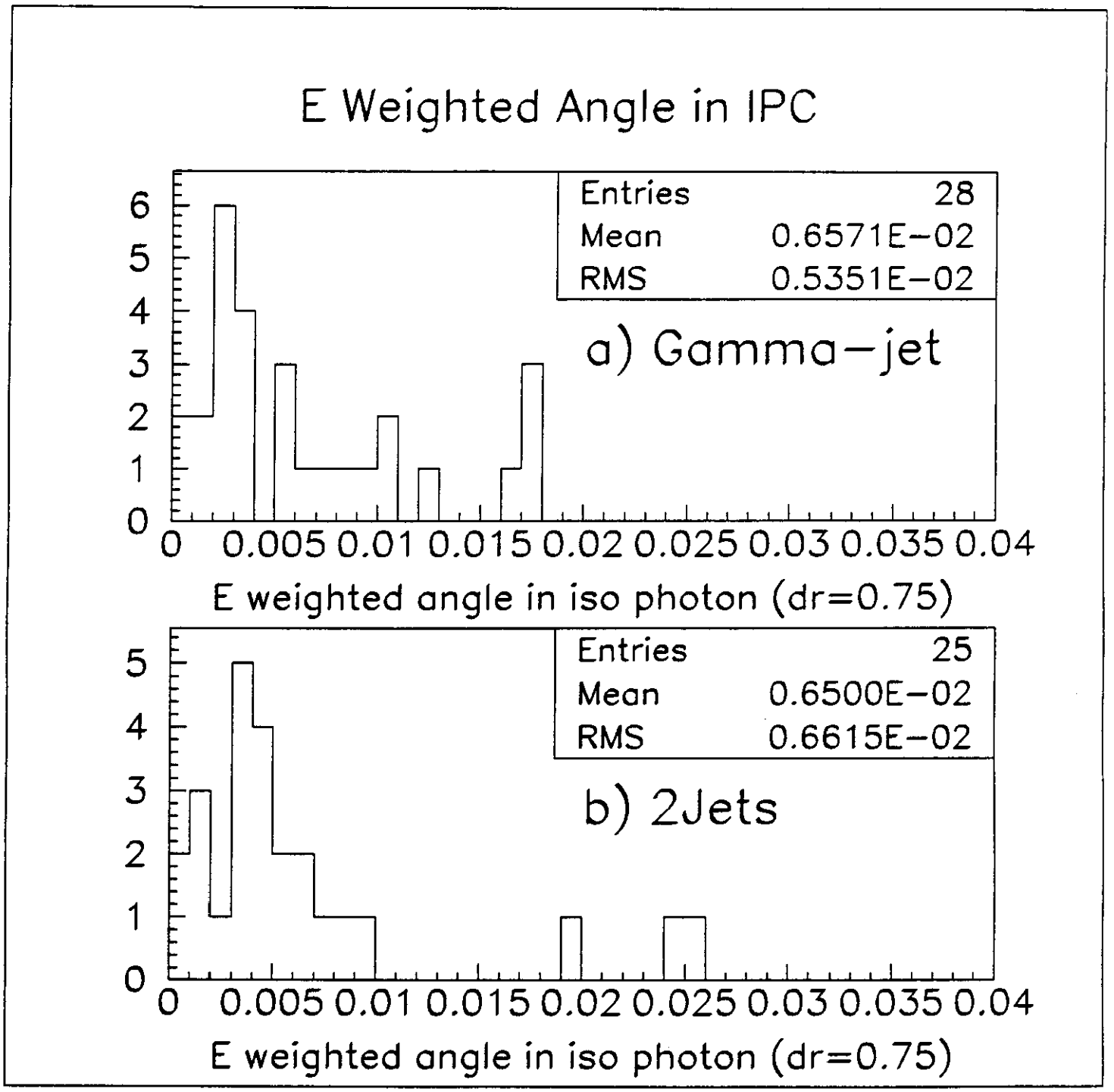

Figure 10: Distributions of $\bar{\theta}$ ofisolated photon candidates, passing an isolation cut of R = 0.75 and E_T^{cut} = 10 GeV from 100k events each of (a) γ-jet and (b) 2jets.

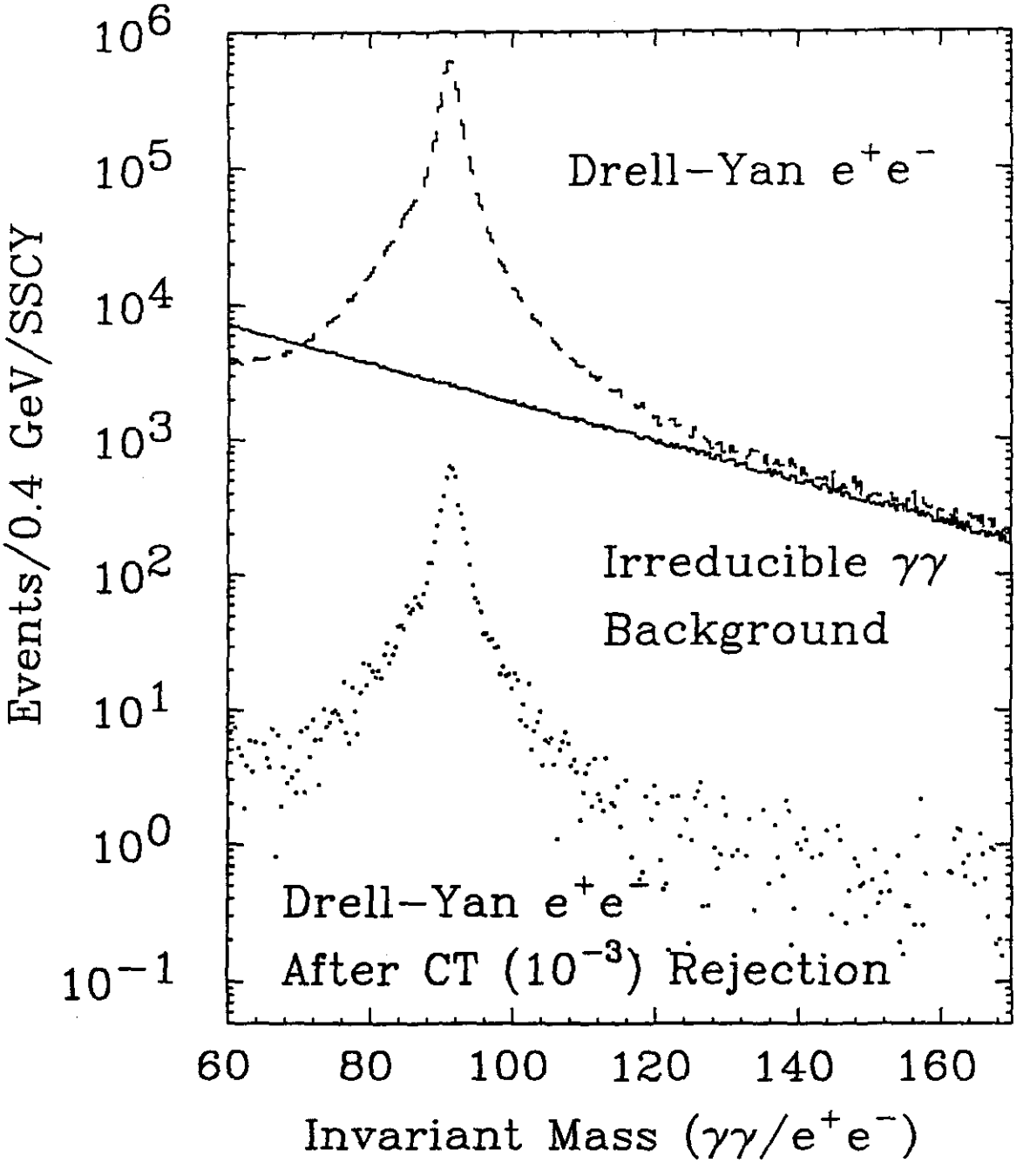

Figure 11: $\gamma\gamma$ and e^+e^- invariant mass distribution of Drell-Yan e^+e^- after event selection cut with no γ/e separation (dashed) is compared with irreducible $\gamma\gamma$ distributions (solid). Also shown in the figure is the Drell-Yan distribution, if 3% of electrons would misidentified as a photon.

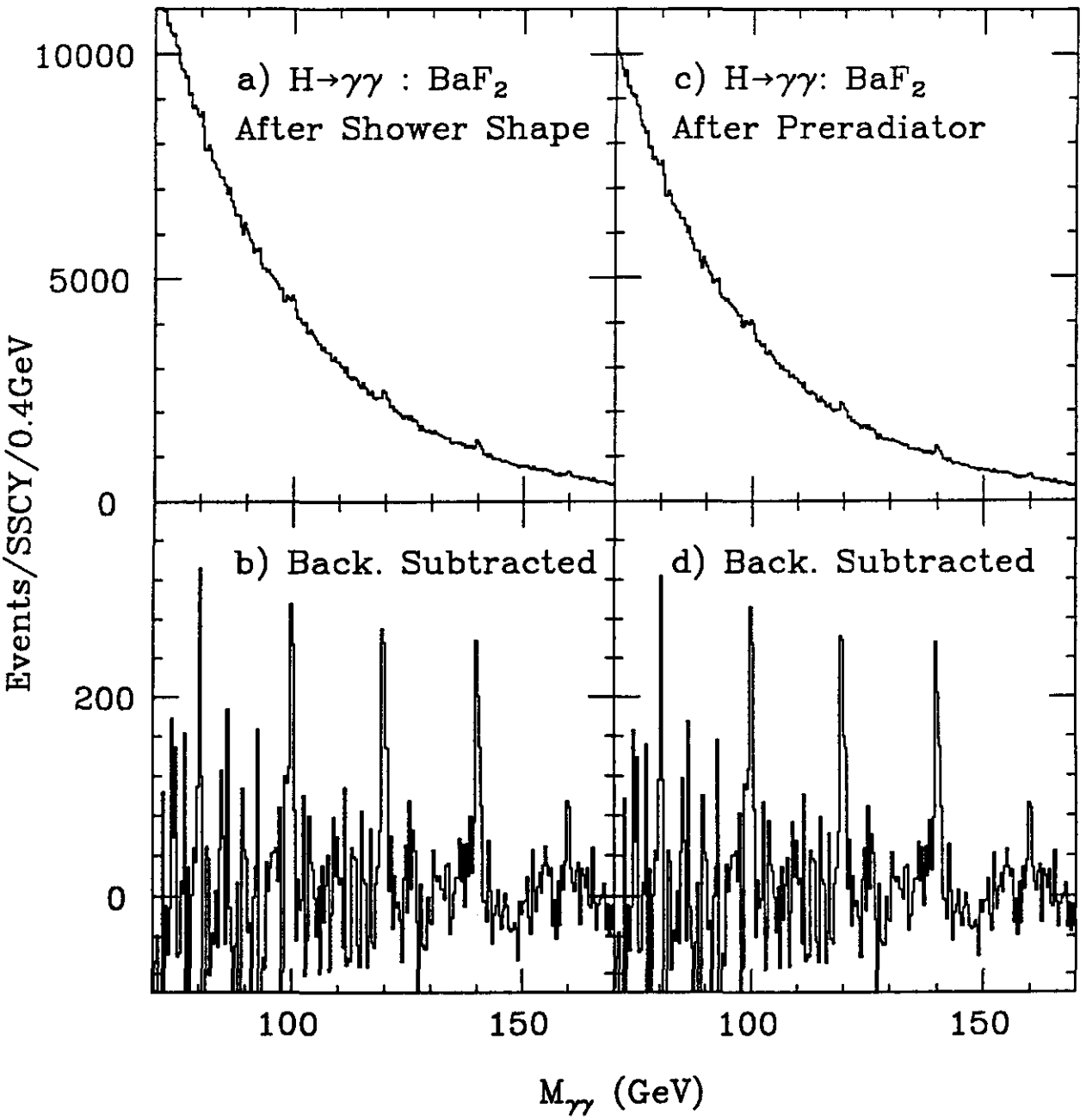

Figure 12: H→ $\gamma\gamma$ signals of 80, 100, 120, 140 and 160 GeV, superimposed on all backgrounds are shown for BaF_2 calorimeter: (a) after shower shape analysis and (c) after preradiator rejection. Corresponding background subtracted spectra are shown in (b) and (d).

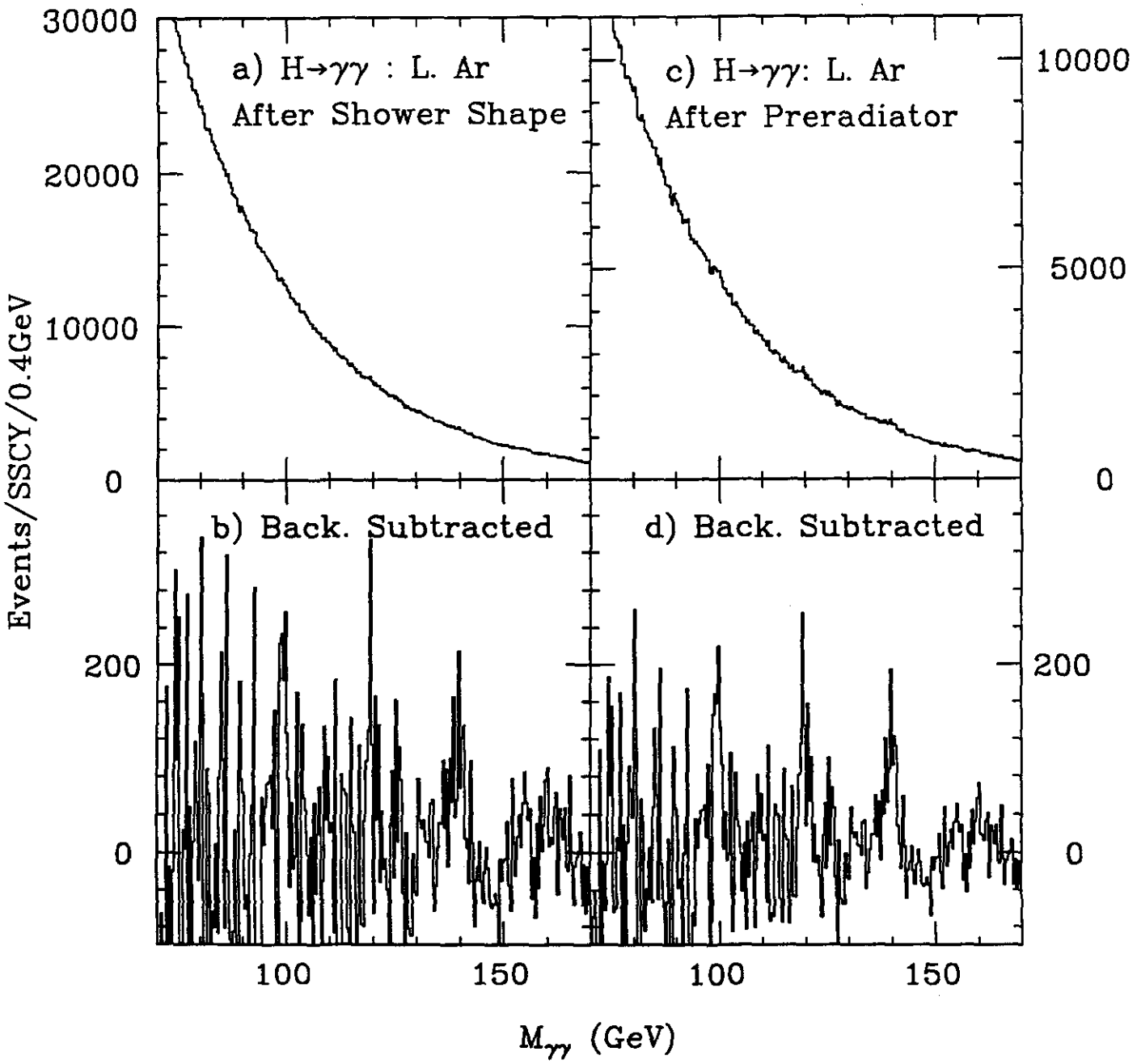

Figure 13: H→ $\gamma\gamma$ signals of 80, 100, 120, 140 and 160 GeV, superimposed on all backgrounds are shown for LAr calorimeter: (a) after shower shape analysis and (c) after preradiator rejection. Corresponding background subtracted spectra are shown in (b) and (d).

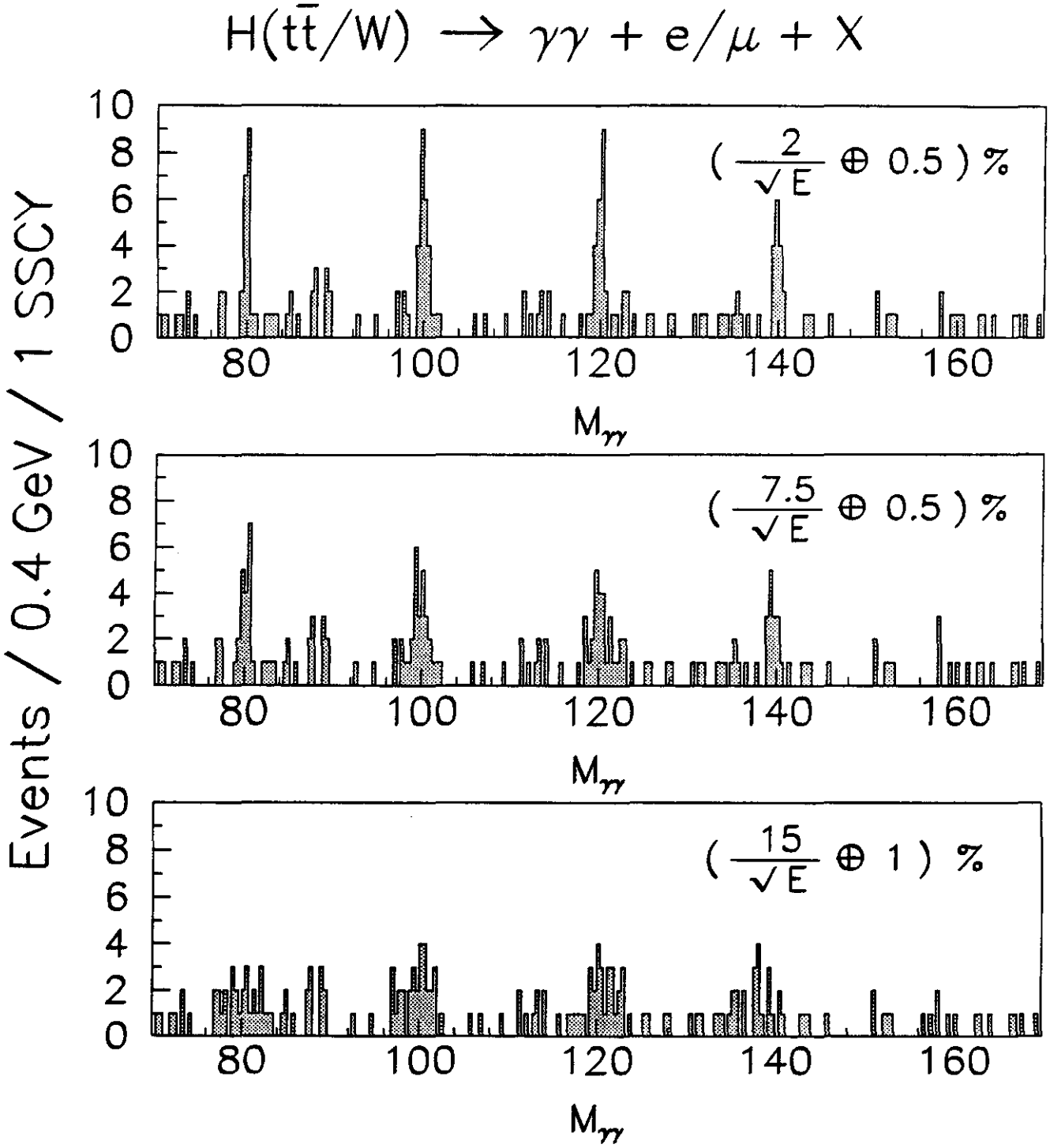

Figure 14: H($t\bar{t}$/W)→ $\ell\gamma\gamma$X signals of 80, 100, 120, 140 and 160 GeV, superimposed on all backgrounds are shown for three different energy resolutions: (a) $(2/\sqrt{E} \oplus 0.5)\%$; (b) $(7.5/\sqrt{E} \oplus 0.5)\%$; and (c) $(15/\sqrt{E} \oplus 1.0)\%$.

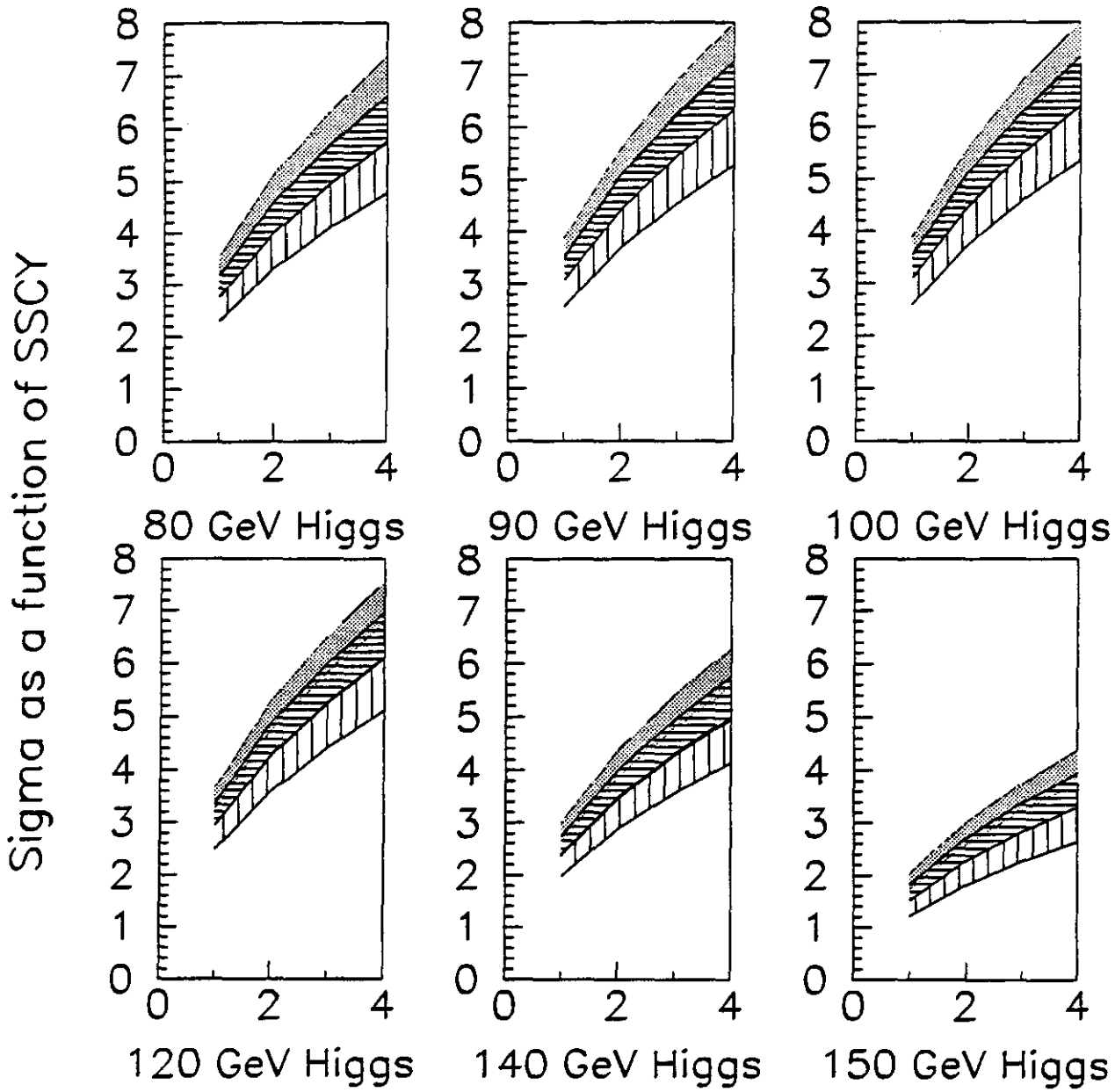

Fig 15. Significance of $H(t\bar{t}/W) \to l\gamma\gamma$ detection as a function of SSCY

Presentation by:

Tomasz Skwarnicki

INTEGRATED FAST-1

Existing detector parametrizations, provided by the subdetector groups, have been integrated into common framework
(In many instances code had to be re-arranged, but "physics" is the same)

Improvements to physics of the simulation:
- bending of charged tracks in the magnetic field (everywhere in the detector)
- decays in flight with generation of secondaries (the same set of particles as in GEANT e.g. $\pi^{\pm}, K^{\pm}, K^{0}_{L}, K^{0}_{S}, \Lambda, \ldots$)
- consistency of responses of various detector subcomponents ensured by tracking each final state particle through the entire detector geometry (one step per subdetector → fast)

of particles through the geometry

"MU"

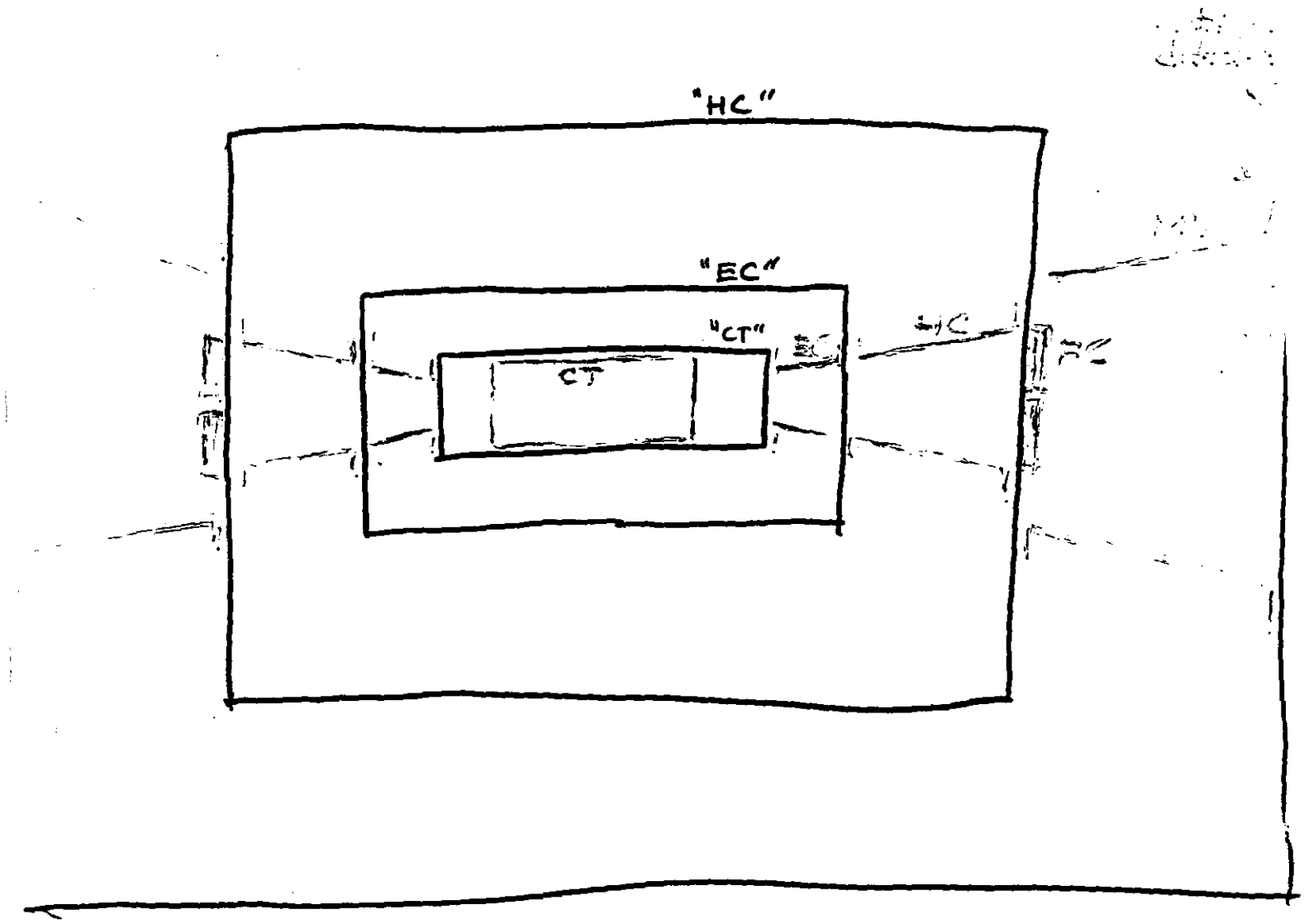

detector geometry structure

(schematic, not in scale!)

CT : detector resolution (momentum, vertex):
CTMEAS

EC, HC: thickness:
CDEPTH
rescaled to true path length along particle trajectory
shower development:
re-arranged code from
CALOED
energy deposition by muons
ELOS
scaled to depth along the trajectory
(optionally code from
MUFAST)
Bremstrahlung fraction taken from
MUFAST
energy deposition by other MIP particles (e.g. π before interaction)
MINION

FC: detector resolution
FCSMEAR

MU: energy loss see above
geometrical acceptance (holes in θ, ϕ)
taken from MUFAST
momentum resolution
RESMAG
detection and trigger efficiencies
MUFAST

ORGANIZATION OF CODE AND DATA

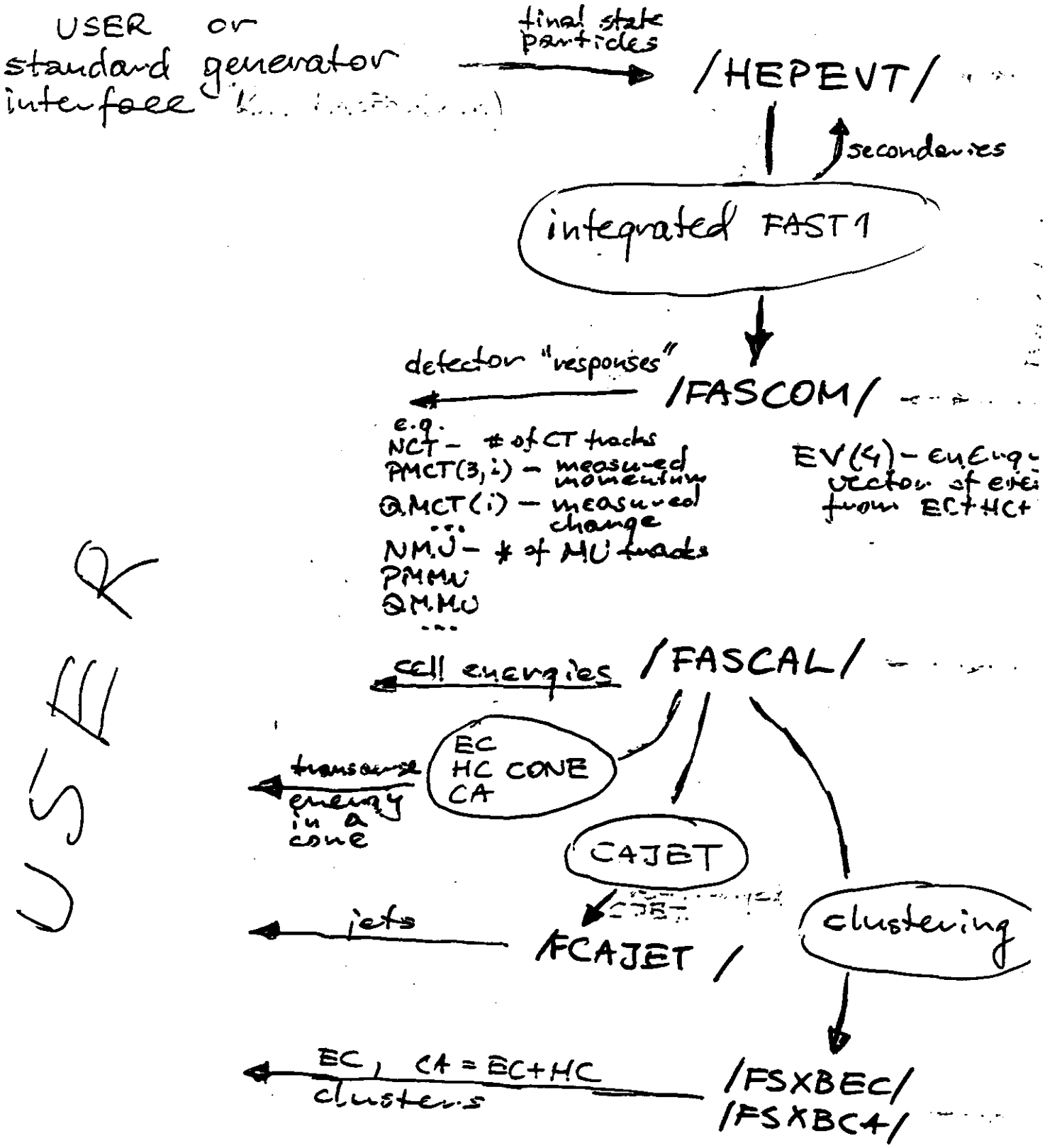

Possible improvements:

- integration of TR routines
- integration of BaF_2 option
- multiple scattering
- γ-conversions in CT
- FAST 2 for up-to-date baseline

...

CHAPTER XX: GEM PHYSICS SIMULATIONS

XX.AA: The FAST1 Model of the GEM Detector

While complete GEANT simulations are important for determining detector parameters, they are far too slow to analyse the large samples of events needed to study signatures and backgrounds, at least at this stage in the evolution of GEM. A much faster simulation, known as FAST1, has therefore been created using established techniques for parameterized simulations. Its purpose is to provide a fast simulation of the gross features of the GEM Baseline 1 detector. This provides an interface to physics event generators and single particle generators. The generated particles are then tracked through each of the major subsystems: the central tracker, the calorimeter, and the muon system, and the response of each is stored in a data structure. Calorimeter and muon triggers are also simulated. Finally, hooks are provided for user analysis code.

An overall framework has been written which calls an event generator and then tracks the particles through the detector, calling in turn each of the subsystem simulation routines. Various support routines are included in the package, including, for example, one for finding jets.

The resulting package is adequately fast, about 3 sec/event on an HP 9000/720, and most of the physics studies reported here are based at least in part on it.

XX.AA.1: Event Generation

Events for FAST1 can be generated with ISAJET [F. Paige and S. Protopopescu], PYTHIA [T. Sjostrand, et al.], or a single particle generator, or events can be read from files in various formats. In all cases, the event information is stored in the STDHEP format [Lynn Garren, FNAL report PM0050], and the STDHEP codes are used for particle types. This allows the same analysis to be used for different generators and should make it simple to incorporate additonal generators in the future.

XX.AA.2: Central Tracker Parameterization

The central tracker is perhaps the most difficult system to parameterize, since its performance depends so much on occupancy. Nevertheless, the occupancy is quite low in the GEM Baseline 1 design, so a parameterization should be sufficient to describe the most important aspects. The FAST1 parameterization includes:

(1) Resolution on momentum, both with and without a vertex constraint, including the expected chamber resolution, bending in the magnetic field, and the effect of multiple scattering;

(2) Resolutions on the impact parameter and the z position of the vertex, based on Gaussian parameterizations of full GEANT simulations of the Baseline 1 design;

(3) Photon conversions and resolution effects from the tracker material as a function of η and ϕ, again based on a full GEANT simulation of the tracker.

The major limitations of the existing FAST1 simulation of the central tracker are that it treats a single particle at a time, so that inefficiencies correlated with the whole event are not properly reproduced, and that inefficiency or additional occupancy from backsplash from the calorimeter is not included. Work on these topics is continuing.

XX.AA.3: Liquid Argon Calorimeter Parameterization

The FAST1 parameterization of the Baseline 1 liquid argon central calorimeter incorporates approximate parameterizations of the energy and position resolution, transverse and longitudinal shower shapes, and pileup and electronic noise.

The calorimeter is taken to be uniformly segmented in η and ϕ, with $\Delta\eta = \Delta\phi = 0.032$ for the electromagnetic (EM) part and $\Delta\eta = \Delta\phi = 0.08$ for the hadronic (HAD) part. This is not exactly correct but is adequate for the central region. Five EM cells are matched to two HAD ones. The energy resolution is taken to be of the form

$$\frac{\Delta E}{E} = \sqrt{\frac{a^2}{E} + b^2}\,.$$

For electromagnetic particles a varies with η from 0.07 to 0.08 depending on the angle of incidence on the accordion structure, and $b = 0.005$. For hadronic particles $a = 0.6$ and $b = 0.05$. Jet resolutions are obtained by summing over the individual particles.

The energy of both electromagnetic and hadronic particles is shared between the EM and HAD sections of the calorimeter, although the subdivisions of each are not taken into account. The sharing is based on the Bock parameterization [R.K. Bock et al. NIM 186(1981)533]:

$$\frac{1}{E}\frac{dE}{dx} = \frac{w}{X_0}\frac{b^a}{\Gamma(a)}s^a e^{-bs} + \frac{(1-w)}{\lambda}\frac{d^c}{\Gamma(c)}t^c e^{-dt}$$

where X_0 and λ are the radiation and interaction lengths of the material, $s = x/X_0$, $t = x/\lambda$, and a, b, c, and d are linear functions of $\log E$. The interaction point is picked according to an exponential distribution, and the above formula is integrated to determine the sharing. Energy is also shared transversely using a parameterization as a sum of exponentials fit to the full GEANT simulation. No fluctuations in shower shape other than the shower starting point are taken into account, so the fluctuations are underestimated.

The position resolution for an EM shower is assumed to be $4.4\,\mathrm{mm}/\sqrt{E}$, based on the full GEANT simulation. The angular resolution has not been simulated, but $100\,\mathrm{mrad}/\sqrt{E}$ is a reasonable estimate.

Finally, thermal noise and pileup are taken into account, treating the latter as an additional noise term. [**CLELAND REF??**] The distributions are taken to be Gaussians with the following mean values:

EM:	thermal	$E = 35\,\mathrm{MeV/cell}$
	pileup	$E_T = 35\,\mathrm{MeV/cell}$
HAD:	thermal	$E = 250\,\mathrm{MeV/cell}$
	pileup	$E_T = 200\,\mathrm{MeV/cell}$

(summed over the longitudinal sections of each part.) Note that thermal noise gives a constant E per cell, whereas pileup gives a constant E_T.

XX.AA.4: BaF_2/Scintillator Parameterization

The BaF_2 calorimeter parameterization in FAST1 is based on a detailed GEANT simulation of its performance. The segmentation is $\Delta\eta = \Delta\phi = 0.04$ in the EM calorimeter and twice that in the HAD calorimeter. The energy resolution is

$$\frac{\Delta E}{E} = \sqrt{\frac{a^2}{E} + b^2}\,.$$

with $a = 0.02$, $b = 0.005$. Transverse and longitudinal shower sharing is handled using a Bock type parameterization with parameters fit to the GEANT results. The thermal and pileup noise are smaller than for liquid argon and so have been neglected.

The hadronic calorimeter simulation uses the same code as the liquid argon simulation with appropriate changes in the parameters.

Most of the physics processes have been studied using the liquid argon parameterization, but a few for which resolution is crucial have been done for both.

XX.AA.5: Forward Calorimeter Parameterization

The principle goal of the forward calorimeter is to measure $\not{E}_T$, so only the p_T resolution has been parameterized. The p_T resolution is determined mainly by the limited angular resolution caused by transverse shower spreading. To determine this resolution, full GEANT 3.14 showers using the standard cuts were generated for single charged pions with $p = 10$, 200, 500, and 2000 GeV distributed randomly over the $3 < \eta < 7$. Each section of the calorimeter was described as a single block of homogeneous material filled with a GEANT mixture of tungsten alloy and liquid argon. The deposited energy was then binned into cells, taking into account the slightly nonprojective geometry of the baseline design, hadronic smearing, e/h suppression, and electronic noise. This energy deposition was then used to calculate the observed $p_{T,\mathrm{in}}$ and $p_{T,\mathrm{out}}$ in and out of the plane of the primary particle. The resolution for $p_{T,\mathrm{in}}$ is shown in Fig. XX.AA-1.

Based on the limited available statistics, a few hundred events per point, the resolution appears to be Gaussian. Therefore, particles in the forward calorimeter were smeared with a Gaussian whose width is determined by interpolation from the calculated points in p_T and η. This has been used only to calculate $\not{E}_T$. Understanding the reconstruction of jets in the forward calorimeter would require a more detailed parameterization of the shower spreading, which is not yet available.

XX.AA.6: Calorimeter Trigger Parameterization

Calorimeter triggers dominate the trigger rate and so have received the most attention. The FAST1 simulation calculates a number of trigger "primitives" from which it can be determined if the Level 1 or Level 2 trigger is satisfied. The electromagnetic cells are combined in 5×5 trigger towers, matched to 2×2 hadronic trigger towers. These trigger towers are also combined 3×3 groups to give 'jet' trigger towers. For these towers, the number of electromagnetic towers above several thresholds, the number of these satisfying an isolation cut, the number of 'jet' towers above threshold, and the number of EM cells above thresholds subject to a hadronic energy test are all calculated and compared with specified thresholds.

An example of such a trigger is the number of EM towers above a threshold of $E_T = 8$, 16, 50, and 80 GeV subject to the requirements that the hadronic energy $E_{T,\mathrm{had}} < 0.1 * E_T$ and that the E_T in the eight neighboring EM towers is less than 7.5 GeV. This is the basic trigger for photons and for isolated electrons.

Little work has yet been done on the Level 3 trigger, which presumably uses a less sophisticated version of the final analysis cuts.

XX.AA.7: Muon System and Trigger Parameterization

The muon resolution was calculated using a GEANT simulation taking into account the detailed Baseline 1 magnetic field, the geometry and expected resolution of the chambers, and multiple scattering in these chambers. No central tracker information was used. This resolution was then parameterized as a function of p_T and η. In FAST1 the resolution is simulated as a Gaussian in $1/p$ with this width. This substantially agrees with the resolution shown in Chap. ???.

Energy loss in the calorimeter was calculated using GEANT with a GEANT mixture of lead and liquid argon including both dE/dx and hard bremsstrahlung. The energy loss distribution was parameterized as a function of p_T and η, and this is used in FAST1 to generate both the muon's energy deposition in the calorimeter and its energy entering the muon system.

The muon acceptance and trigger efficiency was calculated based on a detailed GEANT simulation and parameterized. The simulation took into account the cracks in ϕ and η in the Baseline 1 design, radiation from the muon producing extra hits in the chambers, and the probability that a muon would bend enough to satisfy the trigger criteria for a given threshold. The probability of reconstructing the muon track was also taken into account based on a preliminary reconstruction algorithm.

Finally, distributions of the number and momenta of tracks and their distances and angles from the primary muon were generated using GEANT. These were parameterized and can be used to estimate the efficiency for reconstructing both isolated muons and muons in hadronic jets.

XX.AA.8: Future Developments

The fast parameterization has achieved the goal of allowing for the accumulation of high statistics in a short period of time. However, improvements are needed, especially for studies for the Technical Design Report. The FAST1 simulation will also evolve as the detector evolves. (The version for Baseline 2 will be FAST2) The general techniques being used will be followed. As experimental data and a full overall GEANT simulation become available, the parameterizations will be based on more detailed knowledge. Specific features that should be added are noted:

(1) Central Tracker: Simulation of track reconstruction efficiency, effects of high luminosity, efficiency of finding the correct vertex and probability of of finding a track stub are among features that are needed.

(2) Calorimeter: Integration of the central region endcap with the forward calorimeter is needed to better study $\not{E}_T$ questions. There are two possible "seamless approaches": (1) treating the whole calorimeter as a tabulated response function, as is done now for the forward calorimeter, or (2) treating it with cells and jet finding, but with the $\eta = 3$ transition and the $\eta = 5.5$ edge region given special smearing functions. Each of two approaches has its uses in dmaifferent contexts. Transverse fluctuations should be added in a way that is separate from position resolution.

Fig. XX.AA-1: Single pion resolution for various p and η as calculated from GEANT for the GEM baseline forward calorimeter.

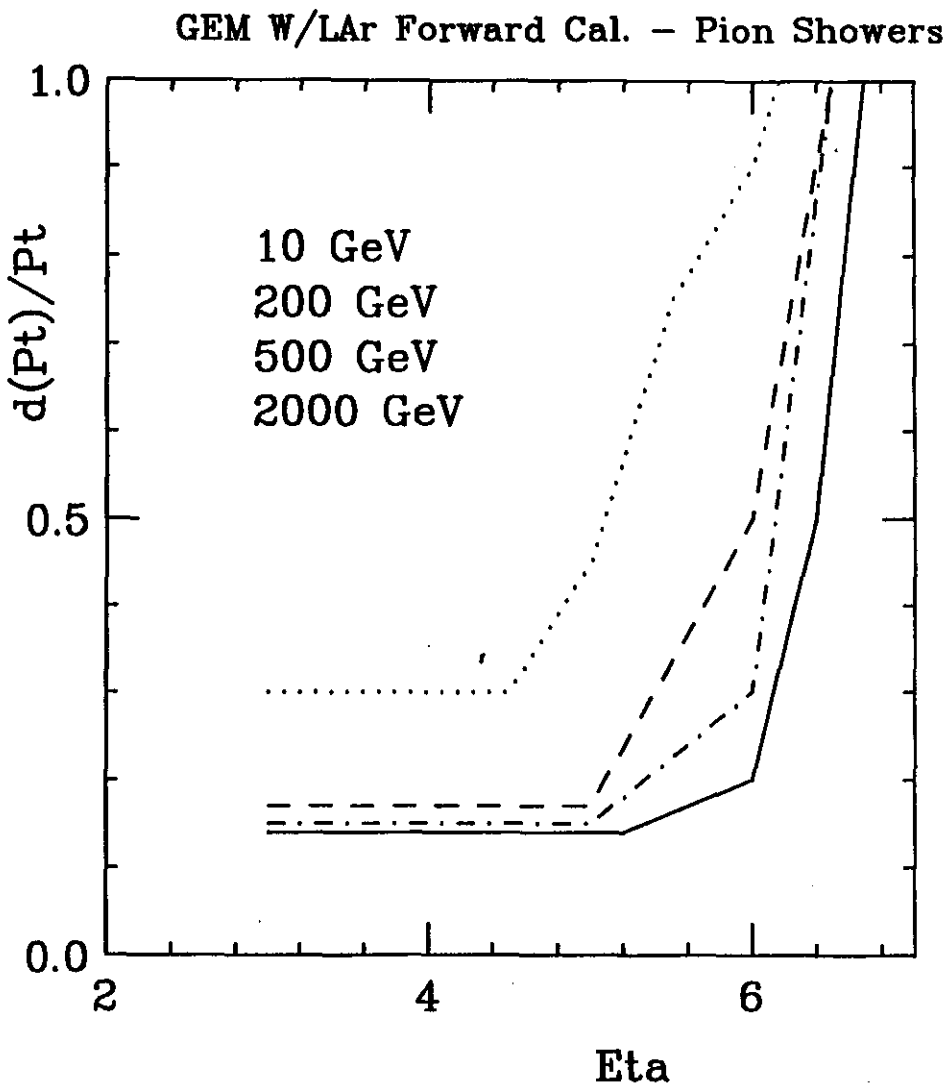
GEM W/LAr Forward Cal. – Pion Showers
1.0
0.5
0.0
d(Pt)/Pt
10 GeV
200 GeV
500 GeV
2000 GeV
2
4
6
Eta

XX.BB: Missing Energy Signals

For a variety of possible SSC physics signatures it is important to measure the missing transverse energy $\not{E}_T$ in the range $\not{E}_T \gtrsim 100\,\mathrm{GeV}$. The forward calorimeter is crucial for this, since without it the $\not{E}_T$ cross section would be dominated by missing jets.

The calorimeter parts of the FAST1 simulation were used for this analysis. For the forward calorimeter, FAST1 calculates a smeared transverse momentum for each particle based on a parameterization of results from a full GEANT simulation. For the central calorimeter it includes the energy resolution, the average transverse shower shape, energy sharing between the electromagnetic and hadronic sections, and electronic noise and pileup. The transverse spreading could cause energy to leak beyond the edge of the calorimeter at $\eta = 3$. This has not yet been included in FAST1, but an earlier GEANT simulation showed that this leakage is well enough measured by the forward calorimeter that it does not significantly degrade the $\not{E}_T$ resolution. [**Forden REF**] Therefore, leakage beyond $\eta = 3$ was assumed to be correctly measured with the usual energy resolution.

XX.BB.1: Search for a 300 GeV Gluino Using Jets and $\not{E}_T$

For the gluino analysis the minimal supersymmetric extension of the standard model (MSSM) was assumed with two Higgs doublets and superpartners of all the standard particles, including four neutralinos $\tilde{\chi}_i^0$ and two charginos $\tilde{\chi}_i^\pm$. If the gluino is lighter than the squarks, then it will decay into $q\bar{q}\tilde{\chi}_i^0$ or $q\bar{q}'\tilde{\chi}_i^\pm$; the $\tilde{\chi}$'s will in turn decay via a cascade until the lightest supersymmetric particle $\tilde{\chi}_1^0$ is reached. This is stable and escapes from the detector, giving a $\not{E}_T$ signature. Other signals such as like-sign dileptons are also possible.

As in the GEM LOI analysis, all of the decay modes were calculated assuming a gluino mass $M_{\tilde{g}} = 300\,\mathrm{GeV}$, a supersymmetric Higgs mass $\mu = -300\,\mathrm{GeV}$, and a ratio of vacuum expectation values $\tan\beta = v_2/v_1 = 2.0$. The squark masses were taken to be 600 GeV. Gluino pair production and decay were simulated using ISAJET 6.43. Since the gluinos will typically be produced with $p_T \sim M_{\tilde{g}}$, one expects a signal with multiple jets plus large $\not{E}_T$. The dominant physics background for this signal comes from missing neutrinos from heavy quarks. It was shown in the LOI that the other physics backgrounds, e.g., $Z \to \nu\bar{\nu}$ at high p_T, are negligible in this mass range, although they do contribute for higher gluino masses. In addition there are detector-induced backgrounds from mismeasured jets.

ISAJET 6.43 was used to generate 10K gluino signal events, including all the decays of the MSSM, and 1.8M QCD jet events distributed in ten bins covering $50 < p_T < 1600\,\mathrm{GeV}$. Other than the minimum p_T of the hard scattering, no preselection of the events to contain real missing energy was made. This is necessary to obtain the correct cross section for

mismeasured jets. All events were run through the FAST1 simulation, $\not{E}_T$ was calculated as described above, and jets were found using a fixed-cone algorithm with $R = 0.7$.

In the inclusive $\not{E}_T$ cross section the background is large compared to the signal. To reduce the background, at least four jets with $p_T > 75\,\mathrm{GeV}$ were required in the central calorimeter. Jets in the forward calorimeter are not used, so its ability to recognize them is not an issue. In addition the sphericity in the transverse plane S_T was calculated from the central calorimeter cells with $E_{T,\mathrm{cell}} > 0.5\,\mathrm{GeV}$, and a cut $S_T > 0.2$ was made. After these cuts the signal to background ratio S/B is about 2 for $\not{E}_T \sim 250\,\mathrm{GeV}$.

Semileptonic decays of gluinos would of course be important to study; for example, isolated like-sign dileptons $\ell^\pm\ell^\pm$ provide a signal for the Majorana nature of the gluino. However, making a lepton veto further improves the S/B for the $\not{E}_T$ distribution. Events were vetoed if they contained a muon or an isolated electron with $p_T > 20\,\mathrm{GeV}$ and $\eta < 2.5$. Isolated electrons were defined by requiring that the total energy in the electromagnetic and hadronic calorimeter in a cone $R = 0.1$ match the momentum, $|E/p - 1| < 0.1$. This effectively combines a HAD/EM cut and an EM/p cut. It is intended to select those electrons which could plausible be identified, mainly those from direct t decay. The efficiency of the lepton identification has not been simulated in detail in this study, but it cannot be very crucial, since even if it were perfect there still would be remaining background from τX decays of b's and t's. The signal and background remaining after these cuts are shown in Fig. XX.BB-1. The ratio $(S + B)/B$ is shown in Fig. XX.BB-2 and reaches about 5 for the GEM baseline calorimeter.

Fig. XX.BB-2 also shows the $(S + B)/B$ ratio obtained using $\not{E}_T$ calculated from the the missing ν and $\tilde{\chi}_1^0$ momenta. While the GEM calorimeter increases the background at low $\not{E}_T$, it provides reasonable agreement with the perfect detector result in the region for which the ratio is large.

The statistical significance of the signal is not an issue. The t, W and Z backgrounds can be checked using isolated lepton samples; the b and c backgrounds can be checked using muons in jets. The $\not{E}_T$ resolution of the detector can be checked using inclusive data on QCD jets and $\gamma +$ jets events. Given all these constraints, the background should be reliably known, so observation of a $\not{E}_T$ cross section 5 times that expected from the standard model should be very convincing.

XX.BB.2: Search for a 300 GeV Gluino Using Jets and $\ell^\pm\ell^\pm$

In addition to the $\not{E}_T$ signature described above, there are many other signatures for supersymmetry. In particular, since the gluino is a self-conjugate Majorana fermion, gluino pairs can give isolated $\ell^\pm\ell^\pm$ pairs. Observing these likesign pairs is essential for

understanding the nature of any $\not{E}_T$ signal.[1] The dominant standard model background is expected to be from $t\bar{t}$ events in which either a $\overset{(-)}{b} \to \ell X$ lepton appears isolated or an isolated lepton sign is wrongly determined. Since the cross section for a 300 GeV gluino is large, one can rely just on $\mu^\pm\mu^\pm$ events, for which the signs are well determined in GEM. Nevertheless it seems useful to see whether $e^\pm e^\pm$ can also be observed in GEM.

ISAJET 6.43 was used to generate 10K events each of the $\widetilde{g}\widetilde{g}$ signal and $t\bar{t}$ background using the same minimal supersymmetric model parameters as in the previous section. The gluino pairs were forced to decay into $\widetilde{W}^-\widetilde{W}^-X$ and thence into e^-e^-X. The $t\bar{t}$ pairs were forced to decay by $t \to b$, $b \to e^-X$, and $\bar{t} \to e^-X$. The additional background from $t\bar{t}$ events in which the lepton sign was wrongly deterimined was found to be small, since the electrons from the gluinos typically have $p_T \lesssim 200$ GeV whereas the tracker provides good sign selection up to $p_T \approx 400$ GeV.

The events were then simulated using FAST1. Pileup and noise at $\mathcal{L} = 10^{33}\,\mathrm{cm}^{-2}\mathrm{sec}^{-1}$ were included using the calorimeter simulation CALOED. Jets were found using CJETS with $R = 0.7$, and at least four jets with $p_T > 40$ GeV in the central calorimeter ($\eta < 3$) were required. Electrons were called isolated if after detector simulation they had an additional hadronic energy $E_{\mathrm{had}} < 5$ GeV in a cone $R = 0.3$, and at least two isolated electrons with $p_T > 10$ GeV and $\eta < 2.5$ were also required. Since this cut was made on total rather than transverse energy, it is quite severe in the forward direction. Isolated electrons were assumed to be identified with perfect efficiency; this is believed to be a reasonable approximation and in any case should affect signal and background equally. Such electrons were removed from the jets found by CJETS by vetoing any jet with $R < 0.5$ from an electron. No cut was made on $\not{E}_T$.

After these cuts, 2212/10000 like-sign pairs from the gluino events and 61/10000 like-sign pairs from the $t\bar{t}$ events survived. When the production cross sections and branching ratios are taken into account and different charges are summed, this corresponds to 6.6×10^4 signal events and 2.1×10^4 $t\bar{t}$ background events accepted per year, giving $S/B = 3.1$ after only minimal optimization of the cuts. Work to refine the cuts is continuing, but it is already clear that GEM can observe a 300 GeV gluino in the $e^\pm e^\pm$ channel.

XX.BB.3: Search for $H \to ZZ \to \ell^+\ell^-\nu\bar{\nu}$

For a standard model Higgs with $M_H \gtrsim 600$ GeV the rate for $H \to \ell^+\ell^-\ell^+\ell^-$ becomes small, and other modes need to be considered. The mode $H \to \ell^+\ell^-\nu\bar{\nu}$ has six times the branching ratio. The most serious background to detection of this mode is from the QCD

[1] H. Baer, et al., Phys. Rev. D45, 142 (1992).

production of Z^0 + jets, and discrimination is based on the $\not{E}_T$ of the event. This makes the measurement very sensitive to the calorimeter coverage at high eta. ISAJET 6.46 was used to generate 10000 Higgs events with $M_H = 800\,\mathrm{GeV}$ and 50000 Z^0 + jets events in the range $50 < p_{T,Z} < 1600\,\mathrm{GeV}$ generated as five samples.

The signal and background events were first analyzed for perfect detector coverage up to $\eta = 5.5$. In this analysis, neutrinos were excluded, and muons were considered to deposit 3 GeV equivalent in the calorimeter. The events were also analysed using the GEM FAST1 simulation routines, which parameterize the response of each detector subsystem as a single particle smearing and acceptance function. Specifically, for this study FCSMEAR was used to give the response in the forward calorimeter, and MUFAST was used to give the muon detector response. The forward calorimeter studied here was the tungsten and liquid argon option associated with the current GEM baseline detector. The full machinery of the central and endcap parameterization, CALO, was not needed because this measurement is insensitive to central calorimeter segmentation, but the CALO energy response functions were used for $\eta < 3.0$. In the current study, only the mode $Z^0 \to e^+e^-$ was analyzed.

The analysis began by reconstructing the Z^0 and making a loose requirement that the mass be within 20 GeV of M_Z. The reconstructed Z^0's were required to have a $p_T >$ 350 GeV and be centrally produced with $\eta < 1.5$. In Higgs events, then, this sample has a large $\not{E}_T$, whereas Z^0 + jets events exhibit jet activity on the side opposite the Z^0. The separation is not perfect because the Higgs events have spectator jets which balance the Higgs p_T, and because in Z^0+jets events the jets occasionally fluctuate to produce high-p_T neutrinos.

To characterize the jet activity, the scalar p_T of all particles in the semi-cylinder opposite the Z^0 is summed. Using this broad angular range allows for the p_T of the Higgs, which is typically of order 100 GeV. This summed scaler p_T is shown for a perfect detector in Fig. XX.BB-3. The signal events lie at low p_T and are uncontaminated by background up to 360 GeV. There are 38 events for one SSC year at $\mathcal{L} = 10^{33}\,\mathrm{cm}^{-2}\mathrm{sec}^{-1}$ up to this cut. The same sample of events is shown after processing with the GEM FAST simulation in Fig. XX.BB-4. The more realistic coverage at high eta has degraded the measurement at low p_T, but it is possible to apply a cut at 120 GeV and have an uncontaminated sample of 22 signal events in one SSC year.

Future work in this area includes study of the liquid-scintillator forward calorimeter option, further optimization of the liquid argon design, study of the $Z^0 \to \mu^+\mu^-$ modes, and finally, using the full GEM GEANT detector simulation to incorporate effects such as p_T crossover in the $\eta \approx 3$ transition region. Backgrounds due to $gg \to ZZ$ and $q\bar{q} \to ZZ$ will also be considered. The emphasis of the current study was to determine the effect of

the p_T response of the GEM baseline design on detection of a massive Higgs in this mode. The baseline design seems adequate to detect the signal with an acceptable tightening of the cuts compared to an idealized detector.

Fig. XX.BB-1: Gluino signal and QCD background vs. $\not{E}_T$ after the jet and sphericity cuts and the lepton veto described in the text.

Fig. XX.BB-2: Solid: Ratio of $(S+B)/B$ from Fig. XX.BB-2. Dotted: Same ratio using $\not{E}_T$ calculated from the ν and $\tilde{\chi}_1^0$ momenta.

Fig. XX.BB-3: E_T opposite $Z \to e^+e^-$ after cuts for 800 GeV Higgs and Z^0 + jets background with perfect calorimeter covering $\eta < 5.5$.

Fig. XX.BB-4: Same as Fig. XX.BB-4 for the GEM baseline calorimeter.

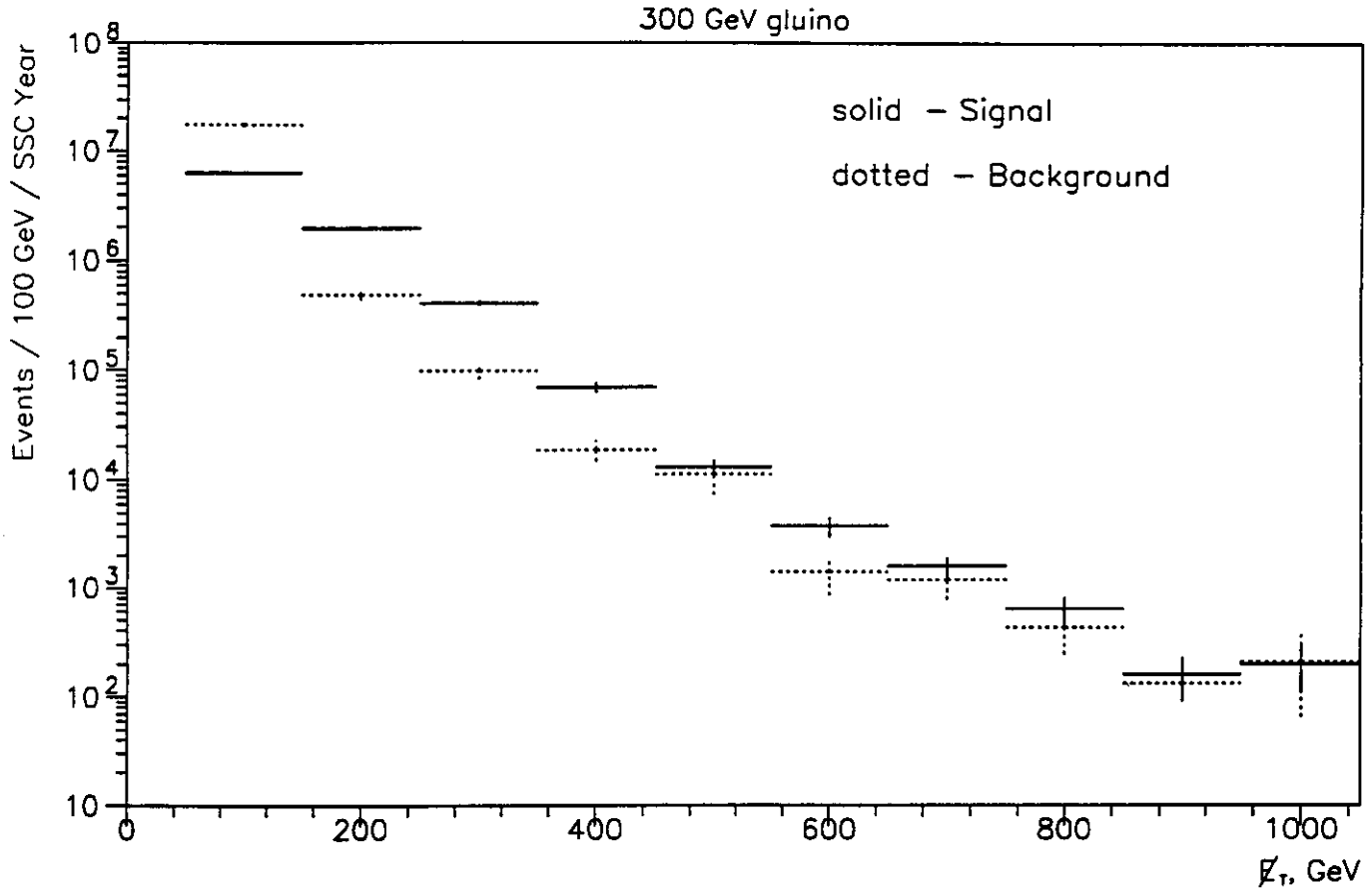
300 GeV gluino
solid – Signal
dotted – Background
Events / 100 GeV / SSC Year
$\not{E}_T$, GeV

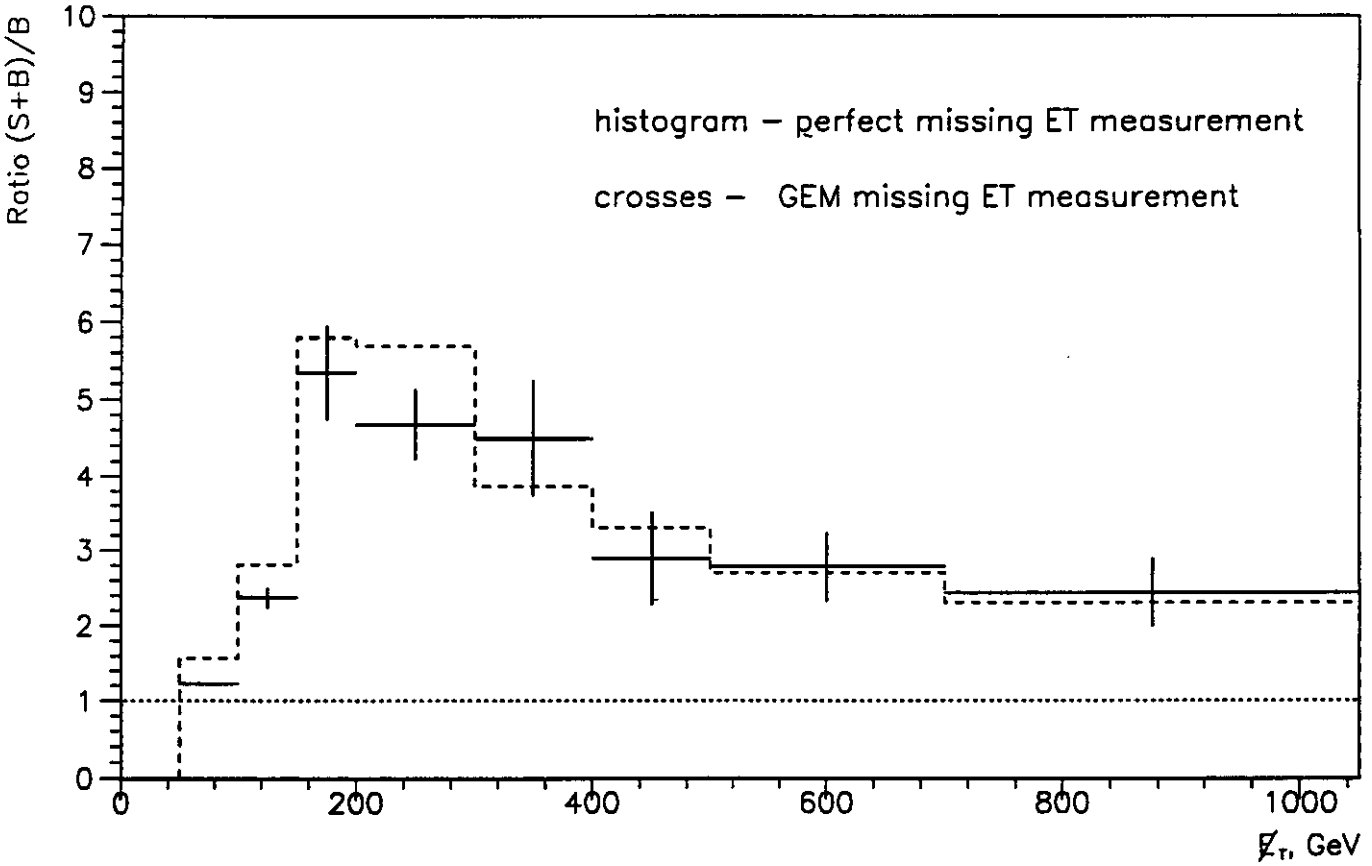
histogram – perfect missing ET measurement
crosses – GEM missing ET measurement
Ratio (S+B)/B
$\not{E}_T$, GeV

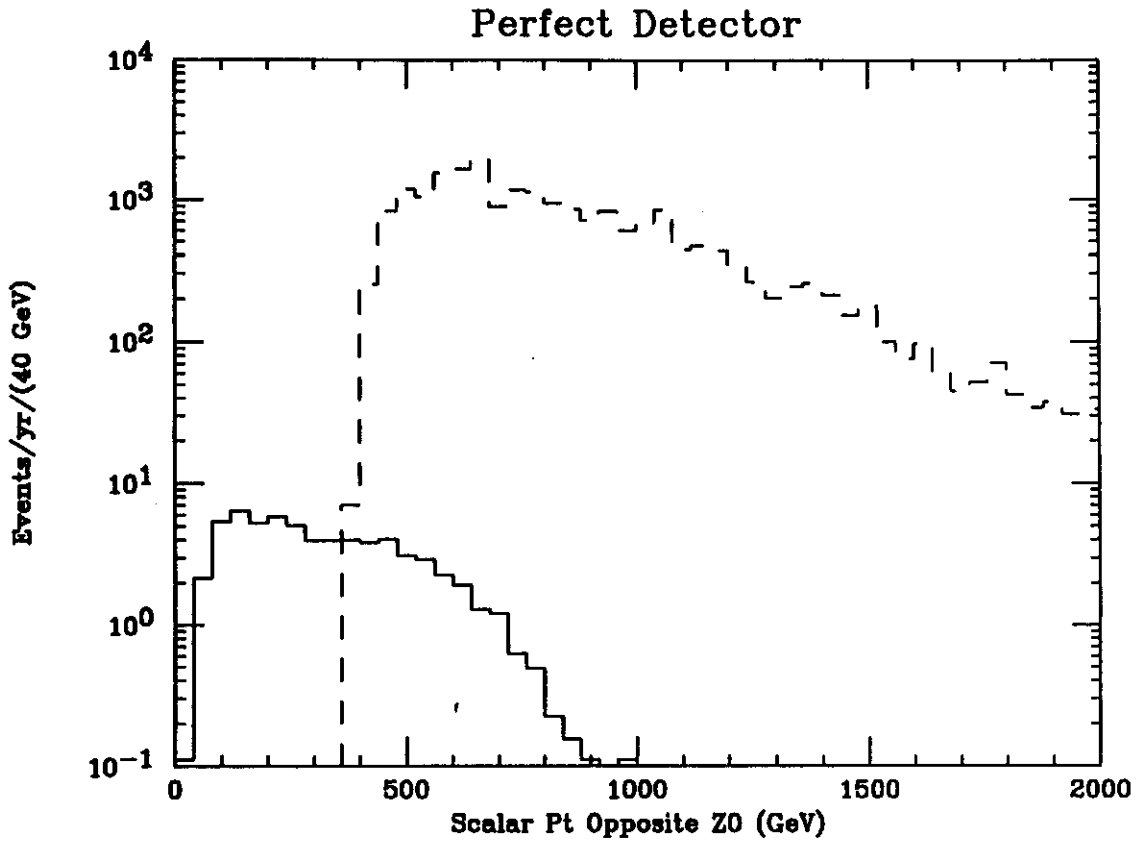
Perfect Detector
Events/yr/(40 GeV)
10^4
10^3
10^2
10^1
10^0
10^{-1}
0
500
1000
1500
2000
Scalar Pt Opposite Z0 (GeV)

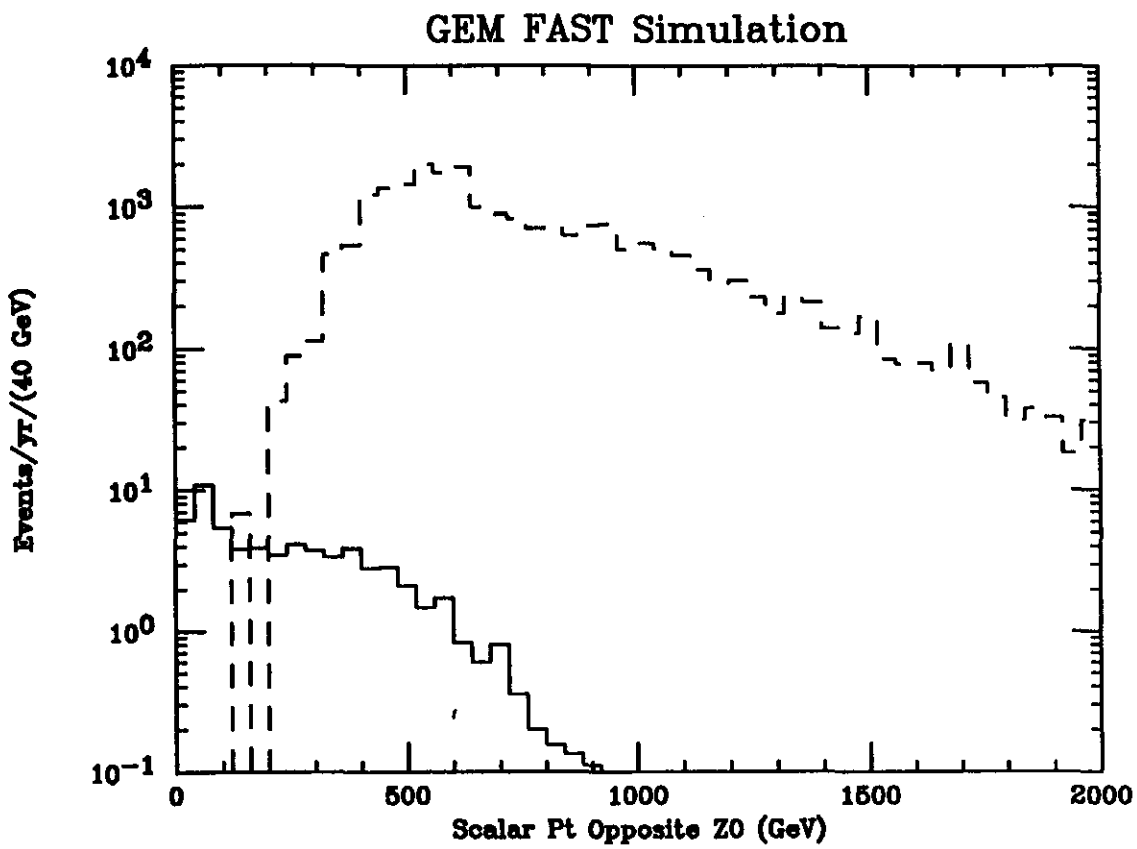
GEM FAST Simulation
Events/pT/(40 GeV)
Scalar Pt Opposite Z0 (GeV)
10^4
10^3
10^2
10^1
10^0
10^-1
0
500
1000
1500
2000

<u>Lessons</u> from FAST1

Must have clear defns. of ~~data stru~~ detailed goals. *

Must define data structures

Must define function of each module

Must modularize

Must use versions; version control

Ability of author to make changes

Agreement of author to respond

Distribution by pull or push acc. to task

* Definitions must precede coding.

Coding rules

documentation

test programs; debugging